Fall 12-15-2016

INFRARED DIAGNOSTICS ON MICRO AND NANO SCALE STRUCTURES

Jitto Titus

INFRARED DIAGNOSTICS ON MICRO AND NANO SCALE STRUCTURES

by

JITTO TITUS

Under the Direction of A. G. Unil Perera, PhD

ABSTRACT

Fourier Transform Infrared spectroscopy is used as a diagnostic tool in biological and physical sciences by characterizing the samples based on infrared light-matter interaction. In the case of biological samples, Activation of Jurkat T-cells in culture following treatment with anti-CD3 (Cluster of Differentiation 3) antibody is detectable by interrogating the treated T-cells using the Attenuated Total Reflection - Fourier Transform Infrared (ATR-FTIR) Spectroscopy technique. Cell activation was detected within 75 minutes after the cells encountered specific immunoglobulin molecules. Spectral markers noted following ligation of the CD3 receptor with anti CD3 antibody provides proof-of-concept that ATR-FTIR spectroscopy is a sensitive measure of molecular events subsequent to cells interacting with anti-CD3 Immunoglobulin G (IgG). ATR-FTIR spectroscopy is also used to screen for Colitis in chronic (Interleukin 10 knockout) and acute (Dextran Sodium Sulphate-induced) models. Arthritis (Collagen Antibody Induced Arthritis) and metabolic syndrome (Toll like receptor 5 knockout) models are also tested as controls. The marker identified as mannose uniquely screens and distinguishes the colitic from the non-colitic samples and the controls. The reference or the baseline spectrum could be the pooled and averaged spectra of non-colitic samples or the subject's previous sample spectrum. The circular dichroism of titanium-doped silver chiral nanorod arrays grown using the glancing angle deposition (GLAD) method is investigated in the visible and near infrared ranges using transmission ellipsometry and spectroscopy. The characteristics of these circular polarization effects are strongly influenced by

the morphology of the deposited arrays. Studies of optical phonon modes in nearly defect-free GaN nanowires embedded with intrinsic InGaN quantum dots by using oblique angle transmission infrared spectroscopy is described here. These phonon modes are dependent on the nanowire fill-factor, doping densities of the nanowires and the presence of InGaN dots. These factors can be applied for potential phonon based photodetectors whose spectral responses can be tailored by varying a combination of these three parameters. The optical anisotropy along the growth (*c*-) axis of the GaN nanowire contributes to the polarization agility of such potential photodetectors.

INDEX WORDS: ATR-FTIR, Infrared Spectroscopy, Dichroism, Photodetectors, Colitis, Serum, Infection, Infrared Diagnosis.

INFRARED DIAGNOSTICS ON MICRO AND NANO SCALE STRUCTURES

by

JITTO TITUS

A Dissertation Submitted in Partial Fulfillment of the Requirements for the Degree of

Doctor of Philosophy

in the College of Arts and Sciences

Georgia State University

2016

INFRARED DIAGNOSTICS ON MICRO AND NANO SCALE STRUCTURES

by

JITTO TITUS

Committee Chair: A. G. Unil Perera

Committee: Didier Merlin

Julia Hilliard

Yiping Zhao

Alexander Kozhanov

Vadym Apalkov

Fabien Baron

Electronic Version Approved:

Office of Graduate Studies

College of Arts and Sciences

Georgia State University

December 2016

DEDICATION

This work is dedicated to those seek a relationship with the Creator through the study of His creation.

"Christ is the visible image of the invisible God. He existed before anything was created and is supreme over all creation, for through him God created everything in the heavenly realms and on earth. He made the things we can see and the things we can't see—such as thrones, kingdoms, rulers, and authorities in the unseen world. Everything was created through him and for him. He existed before anything else, and he holds all creation together. Christ is also the head of the church, which is his body. He is the beginning, supreme over all who rise from the dead. So he is first in everything. For God in all his fullness was pleased to live in Christ, and through him God reconciled everything to himself. He made peace with everything in heaven and on earth by means of Christ's blood on the cross." – ***Colossians 1:15-20***

ACKNOWLEDGEMENTS

I would like to express my gratitude to my advisor, Dr. Unil Perera, for his vision, clarity of thought and support that made this work possible. I would also like to thank my committee members: Dr. Julia Hilliard, Dr. Yiping Zhao, Dr. Didier Merlin, Dr. Alexander Kozhanov, Dr. Vadym Apalkov and Dr. Fabien Baron. I would also like to thank Dr. Zetian Mi and his group for his collaboration. My gratitude goes to my colleagues, Dr. Yan Feng Lao, Dr. Gamini Ariyawansa, Dr. Manmohan Singh, Dr. Steven Matsik, Dr. Divya Somvansi, Dr. Ranga Jayasinghe, Dr. Duleepa Pitigala, Dilip Chauhan, Dimuthu Obeysekera, Yigit Aytac, Ismet Glen and Gregory Rothmeyier. I gratefully acknowledge the funding of all my research work partly or in full by the Molecular Basis of Diseases Area of Focus at GSU, US Army (W911 NF-15-1-0018) and AFOSR: 55655-EL-DURIP. Most of all, I am grateful for my lovely bride, whose patience is unfathomable.

TABLE OF CONTENTS

LIST OF TABLES

LIST OF FIGURES

1 INTRODUCTION

One of the conundrums facing today's experimental scientists is the *observer effect[1]* which refers to the alterations induced in the subject by the very act of observing it. From our knowledge of the fundamental physical laws, it is impossible to overcome the observer effect, however we have been able to minimize it. The use of infrared (IR) radiation to observe matter is one such example. IR region, as discovered by Sr. William Herschel (1800) exists between visible light (700 nm) and microwave radiation (1 mm). As a result of the vibrational and rotational states of molecules, IR radiation is emitted and absorbed. As opposed to x-rays, IR is non-ionizing and also has low energy (1.24 meV to 1.7 eV) making it an excellent candidate for use in observing both physical and biological matter without compromising its integrity.

As our foray into natural sciences advances, so does the technology used to understand them. Infrared spectroscopy, which is the study of interaction between IR radiation and matter, has become an indispensable tool for material characterization and diagnostics. The paramount components for spectroscopy are source, detector and the optics required to manipulate infrared light such as an interferometer/dispersive element, mirrors, filters, polarizers etc. IR radiation emitted from a blackbody or other sources can be absorbed by materials if the energy of the photon matches with the resonant frequency of a vibrational mode of the molecules making up the matter. In such a case, there is a transfer of energy from the photon to the molecule causing it to vibrate. Specifically, for a molecule to be IR active, the radiation must cause a change in the dipole moment of the molecule. Since the molecular vibrations are quantized, by knowing the characteristics of the radiation before and after passing through the material of interest, one can diagnose the composition of the material by studying the frequencies of radiation absorbed by it. There are primarily two methods of IR spectroscopy namely, dispersive and interferometric techniques. In

dispersive spectroscopy, the electromagnetic radiation is chromatically dispersed by means of dispersive devices such as a grating or prism. The spatially separated frequencies are consecutively made to pass through the sample and collected by a photodetector. In contrast, interferometric technique involves passing all the frequencies simultaneously through the sample. The infrared diagnostic research mentioned in this dissertation is primarily interferometric due to their inherent advantages outlined in the following sections.

The cornerstone of Fourier Transform Infrared (FTIR) spectroscopy is the interferometer which is an optical device that combines two beams which is then collected by a photodetector. As dictated by the principle of superposition, when two waves of the same frequency are spatially combined, an interference pattern is obtained which is determined by the phase difference between them. This pattern or interferogram, which is in the spatial domain as collected by the detector, is converted into frequency domain by applying the Fourier transform algorithm[2]. This allows one to obtain a spectrum graph of all the frequencies simultaneously without separating them into individual frequencies. A typically used Michelson interferometer is shown in figure 1.1. Infrared beam from a black body source is made to pass through a beam splitter which equally separates the beam into two arms A and B. While beam in arm A is reflected off a fixed mirror and the other (arm B) reflects off a movable mirror. The two beams are then made to spatially overlap as they meet again at the beam splitter. By moving the mirror on arm B, a path difference is introduced between the two beams. Hence an interference pattern is obtained due to the imposed phase differences between the two combining beams. The intensities of the individual frequencies of light modulates as a function the position (or time) of the mirror on arm B due to constructive and destructive interference.

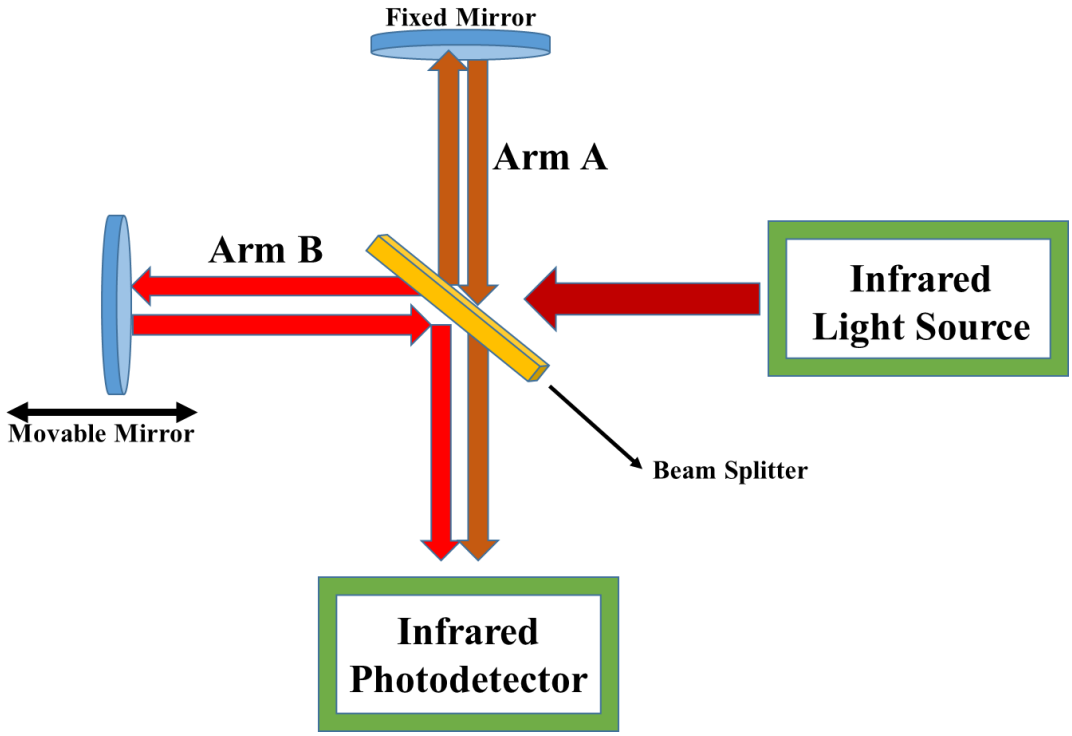

Figure 1.1 *Michelson Interferometer: Infrared radiation coming from the source is equally split by the beam splitter and combines again after reflecting off a fixed and a movable mirror in arms A and B respectively. The superimposed beam is collected by the infrared photodetector and stored as an interferogram.*

Therefore an interferogram is obtained for each position or instance of the mirror movement. In order to optically characterize a material, an interferogram is obtained first without the sample and then with the sample placed between the interferometer and the detector. The ratio of the two interferometric spectra reveals the characteristic absorbance or transmittance of the sample. However, the spectrum thus obtained is in the spatial domain. An algorithm called the Fourier transform (equation 1) converts the spectrum to frequency domain.

$$F(\omega) = \int_{-\infty}^{\infty} f(x) e^{-i\omega x}\, dx \tag{1.1}$$

Where, x is the position of the mirror and ω is the frequency of the IR radiation.

FTIR spectroscopy has three major advantages[3] over dispersive counterpart and they are:

Fellgett's advantage: Since the spectral information is collected from all the frequencies simultaneously (multiplex), the signal to noise ratio is significantly improved compared to the dispersive counterpart when considering the same time period. By averaging the scans over given time, the signal to noise ratio increases by the square root of the scan number.

Jaciquinot's advantage: In monochromator based spectrometers, the dispersed light is spatially separated by slits which greatly reduces the intensity. This is circumvented in interferometric spectrometers as the only limiting factor to the throughput is the collimation efficiency of the light entering the interferometer.

Connes' advantage: A helium neon laser is used to calibrate the frequency scale by passing the laser beam through the interferometer along with the infrared source light. The fringes obtained due to the laser which is dependent on the resolution, is used to calibrate the scale. This provides increased stability and accuracy as opposed to the accuracy of the mechanically moved dispersive element in monochromators.

When the electric field of light oscillates in one direction, it is called as linearly polarized light. A combination of orthogonal linear polarized light gives rise to circularly polarized light when there is a phase difference of 90 degrees. The phase retardation between the two interfering waves dictates the handedness of light i.e. left or right. Circular dichroism[4] (CD), a differential absorption of the left and right circularly polarized light, is a simple yet a powerful vehicle for characterizing some aspects of optical activity in organic and inorganic molecules. In almost all naturally occurring organic materials, there exists asymmetries in all scales down to the molecular level. This asymmetry refers to their incompatibility when superimposed. These molecules are called enantiomers[5]. Macromolecules[6] such as proteins are sensitive to their environment

(temperature, mechanical stress, pH etc). By determining the CD of the protein secondary structures[7], one can extract information even as far as to understand the etiologies of diseases. CD phenomenon is useful in areas such as defense against bioterror[8], detection of manmade objects and bioweapons (military), studying star formations[9] (astronomy), signal transmission[8] (communications) etc. This mandates the development of circular dichroic materials that are not only efficient, but also scalable and nano-sized for easy adaptability to existing imaging technology. Such a nanostructured chiral metamaterial (silver nanorods) is discussed in chapter 2. The eventual need regarding the afore discussed technologies is to be fashioned into portable devices, making the reduction of the footprint of such devices a supreme criterion. One of the key factors that will enable this effort is the capabilities of the IR detectors in terms of the efficiency (detectivity), reduced form factor with the possibility of operation at room temperature. Our Optoelectronics group has developed such detectors with high detectivity[10] (D*) including room temperature detectors[11,12] such as Tunneling (self-assembled) Quantum Dot IR[13,14], (colloidal) Quantum dot capacitor-type[15] and split-off band[16,17] photon detectors. Such devices are also based on micro and nano structure systems allowing the reduction of the form factor. More importantly, in scenarios where specific spectral signatures have been identified to make a diagnosis such as infection or diseases like cancer in biological samples, detectors can be designed so that they are only sensitive to the specifically identified spectral regions of interest. Such examples of multi-band detectors[15,18,19] have also been developed by our group. An important criterion for infrared detectors is reduced footprint and the ability to tailor the wavelength response. A novel candidate meeting this criterion, namely quantum dot embedded nanowire semiconductor structure[20], is posited and discussed in chapter 3.

One of the best detector known to mankind, considering all the technological advancements, is still the living cell[21,22]. In the event of an assault on the cell by means of microbes, allergens or chemical toxins, it develops singular mechanisms of defense[23] which are specific and unique to the assailing agent. By interrogating the cell[24], one can accumulate wide-ranging information such as the identity of the pathogen, its biological surrounding and even the immediacy of its own death. Attenuated total reflectance (ATR) FTIR is a uniquely suited tool of interrogation for biological cells as outlined in chapter 4.

A pressing need for maintaining a healthy life without compromising its quality is point of care diagnostic tools. The successful tool will be minimally/non -invasive, inexpensive, low-risk and portable. ATR-FTIR is an excellent candidate for monitoring and screening[25] for biological conditions. One such debilitating condition is the Inflammatory Bowel Disease (IBD) which keeps steeply increasing in the first world countries. People with ulcerative colitis (UC), a subset of IBD is considered to be at a higher risk for developing colorectal cancer. In chapter 5, FTIR spectroscopy is described as a potential screening tool that can distinguish colitis from other inflammatory conditions.

As *scientific knowledge* in each field of technology and research forges ahead, they also begin to speciate and isolate from other neighboring fields of study. Ironically, *scientific wisdom* suggests that the solution to some problems in a super specialized field of research is not actually contained within, but rather without. Infrared spectroscopy is one such example of a routinely used tool in one field (molecular vibration analysis) being the solution to a problem in other seemingly unrelated fields (biomedical sciences, solid state imaging, metamaterials etc). Future work extrapolating the research described in this dissertation will be discussed in chapter 6.

2 HELICAL NANOROD METAMATERIAL FOR LIGHT MANIPULATION

The circular dichroism of titanium-doped silver chiral nanorod arrays grown using the glancing angle deposition (GLAD) method is investigated in the visible and near infrared ranges using transmission ellipsometry and spectroscopy. These films are found to have significant circular polarization effects across broad ranges of the visible to NIR spectrum, including large values for optical rotation. The characteristics of these circular polarization effects are strongly influenced by the morphology of the deposited arrays. Thus, the morphological control of the optical activity in these nanostructures demonstrates significant optimization capability of the GLAD technique for fabricating chiral plasmonic materials.

2.1 Introduction

Chiral metamaterials[26,27] have the ability to rotate the plane of polarization of electromagnetic waves while minimally absorbing the light. These chiral metamaterials also selectively transmit left or right circular polarized light. The significance of these optically active metamaterials have increased since the prediction of phenomena such as negative refraction and negative reflection[28]. Moreover, they find diverse applications like differentiating enantiomers in analytical chemistry[29], identifying protein conformations in life sciences[30], bioweapon[31] and missile detection[32] in defense, etc.

Glancing Angle Deposition[33] (GLAD) is a vapor deposition technique that proves to be a simple yet scalable method which can be used to fabricate arrays of plasmonic nanostructures [34,35]. Silver has the lowest damping rate, taking into account the scattering due to electron-electron and electron-phonon interactions and lattice defects. Of all the known metal or metal-like materials, in the visible and near infrared region, silver is one of the best candidates for plasmonic devices[36]. Silver, and noble metals in general, are difficult to use with the GLAD technique due

to the high mobilities of surface adatoms, making it difficult to sculpt the materials into asymmetric shapes necessary for chiral metamaterials. However, several techniques have recently been developed that enable the fabrication of chiral noble metal nanostructures using GLAD.[37-40] Of these, titanium-doped Ag helices are particularly interesting, as they are among the simplest to fabricate and their morphological properties are easily tuned.[41] Furthermore, they exhibit intense circular dichroism in the visible region. While the results for the visible region are impressive, characterization of the chiral optical properties of the Ti-doped Ag helices is incomplete, especially in the near-infrared wavelength regions that are important for telecom and biomedical applications. This report investigates the optical properties of Ti-doped Ag helices in the visible and near infrared ranges using transmission ellipsometry and spectroscopy.

2.2 Experimental details

The morphological control of the optical activity in these nanostructures demonstrates the significant optimization capability of the GLAD technique. Silver chiral nanorod structures[41] (CNS) have been grown using a dynamic shadowing growth method, a type of GLAD technique which is further explained elsewhere[33]. In this method, quartz substrates were mounted inside a vacuum deposition chamber on six independently rotating holders, where each holder rotates azimuthally at different speeds, producing six sets of chiral nanorods with different morphological parameters. These samples are labeled, CNS 1 – 6, where CNS 1 rotates the fastest and CNS 6 rotates the slowest. The rotation direction also alternates, CNS 1, 3 and 5 rotated in a clockwise manner throughout the deposition, while CNS 2, 4 and 6 rotated in a counter-clockwise manner. The Ag:Ti vapor flux, obtained by dual-source electron beam evaporation, is made to be incident on these substrates at a large angle (~87^0) with respect to the incident flux, where the vapor incident angle is accomplished by tilting the substrate holder. The vapor flux is maintained at a nominal

5% volume ratio of Ti to Ag throughout the deposition process, and each of the fluxes are monitored by separate quartz crystal microbalances.

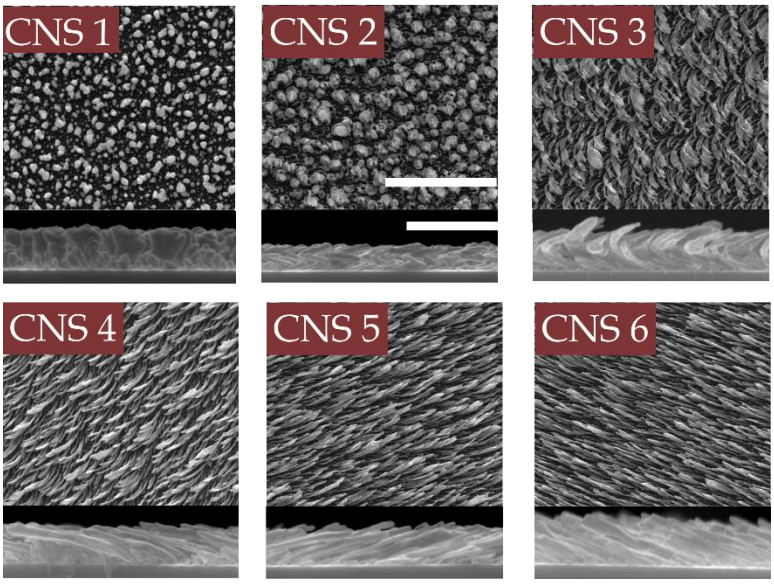

Figure 2.1 *Scanning electron microscope images of Ag:Ti composite chiral nanorod structures CNS 1 to 6. In each of the six images, the upper portion represents the top view and the lower portion, the cross sectional side view of the samples. The scale bars in the top and side views are 2 µm and 500 nm.*

Due to slightly different positions within the chamber, there are slight differences in the Ti/Ag ratios at each of the holders, but these differences are less than ±5% of the Ti/Ag ratio for holder number 3. The nominal five percent Ti atoms used in the vapor mix serves as a barrier to prevent the surface diffusion of silver adatoms, and therefore allows for the sculpting of chiral nanorod arrays. Scanning electron microcopy images of samples CNS 1 to 6 are shown in **figure 2.1** with both top and cross-sectional side views. As is evident from the images, the dimensional parameters of the samples such as density, radius of curvature, height, pitch and the diameter of nanorod, vary with respect to the speed of rotation of the sample stages.

The measured average values of these morphological parameters for the CNS samples are listed in **Table 2.1**. In general, the samples change from post-like structures (CNS 1) to full helices

(CNS 2) to partial helices (CNS 3 – 6) as the substrate rotation speed decreases. In other words, the radius of curvature of the chiral structure is indirectly proportional to the speed of the sample rotation with CNS 1 having the smallest to CNS 6 having the largest radius of curvature.

Table 2.1 *Morphological parameters of the chiral nanorod samples that vary with the sample stage rotation rate. The pitch and radius of curvature increases from CNS 1 to 6 as the sample rotation rate decreases.*

	Height (nm)	**Diameter (nm)**	**Density ($1/\mu m^2$)**	**Radius of Curvature (nm)**	**Pitch (nm)**
CNS 1 (fastest rotation rate)	160 ± 60	N/A	52	N/A	N/A
CNS 2	110 ± 30	30 ± 10	37	90 ± 20	100 ± 5
CNS 3	240 ± 20	50 ± 30	18	260 ± 30	560 ± 50
CNS 4	200 ± 50	40 ± 10	13	540 ± 20	900 ± 200
CNS 5	200 ± 20	50 ± 20	19	1120 ± 90	1900 ± 200
CNS 6 (slowest rotation rate)	220 ± 20	40 ± 10	18	2000 ± 200	4200 ± 400

On the other hand, the pitch of the samples increases as the rotation speed decreases, as expected. The density or the packing factor of the nanorods, as measured through SEM analysis, do not vary greatly except for samples CNS 1 and CNS 2 as there are more bifurcations and coalescing of the nanorods. Overall, the morphology is consistent with growth processes where there is competition between surface diffusion and atomic shadowing.[42] The absorbance spectra of the CNS samples (obtained using J. A Woolam M-2000 ellipsometer) as seen in **figure 2.2** indicate that the CNS samples with faster rotation speeds (CNS1, CNS2 and CNS3) have stronger local surface plasmon resonance absorption modes than the samples with slower rotation speeds

(CNS4, CNS5 and CNS6). The absorbances are averaged for each sample by rotating the sample azimuthally.

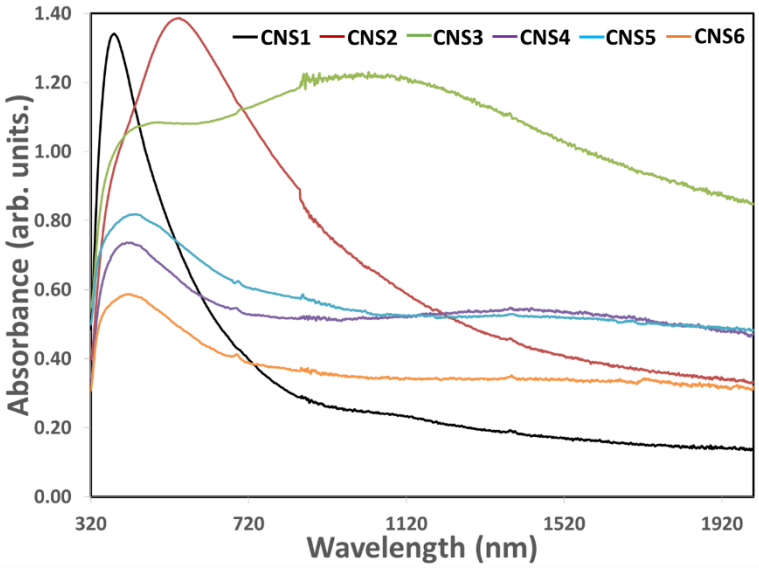

Figure 2.2 *Absorbance spectra CNS samples indicating stronger local palsmon resonance absorbances in samples with faster growth rotation speeds (CNS1, CNS2 and CNS3) than those with slower growth rotation speeds (CNS4, CNS5 and CNS6).*

Transmittance spectra were obtained using a grating spectromenter (USB4000) while rotating the sample azimuthally with respect to the electirc field vector of the incident linear polarized light. The data displayed as a radar plot (figure 2.3) indicates a strong dependence of the linear dichroism on the wavelength for CNS2-6 while CNS1 did not show any dichrosim as expected. Circular dichroism measurements were done using transmission ellipsometry (J.A. Woollam M-2000, 370 – 1000 nm) for the visible region and FTIR spectroscopy (Bruker Vertex70, 900 – 2000 nm) for the NIR regions while averaging over different azimuthal orientations. Circularly polarized light obtained by sending light through a holographic KRS-5 wire grid linear polarizer (Thorlabs WP50H-K) followed by an achromatic broadband flat retardance (Thorlabs AQWP05M) quarter wave plate in the FTIR sample compartment is incident on the sample.

Having the fast axis of the quarter wave plate at +45 and -45° to the linear polarizer produced right and left circularly polarized light respectively.

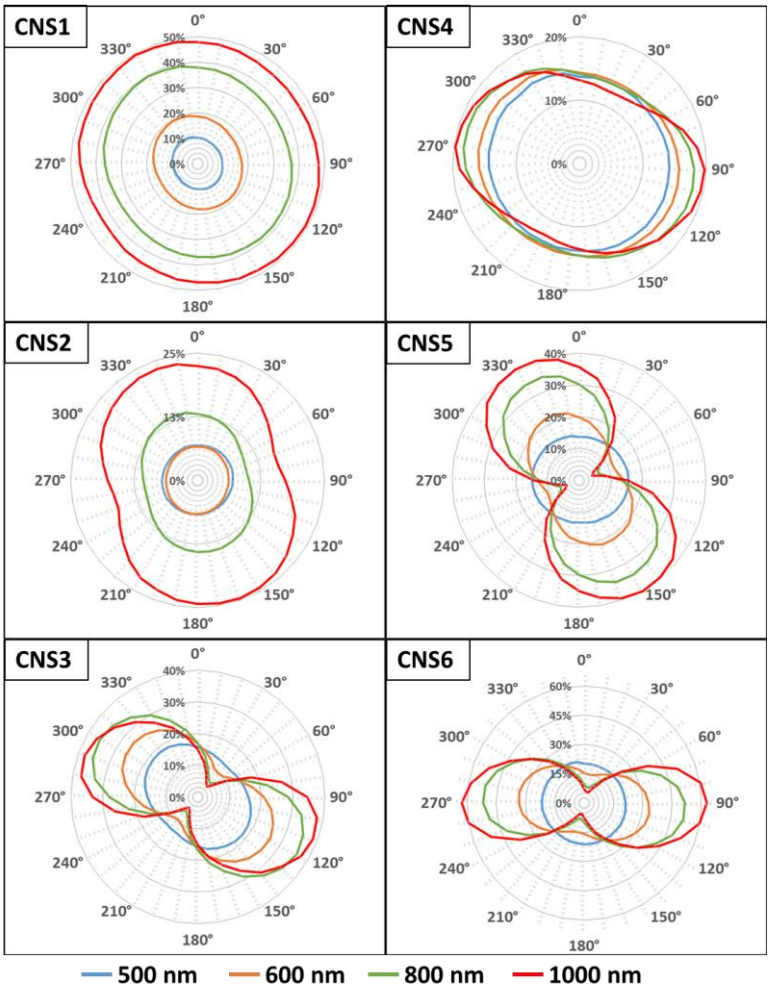

Figure 2.3 *Polarized transmittance radar plot indicating the attenuation of the incident light as the sample is rotated azimuthally with respect to the electric flield vector of the polarized light. CNS1 does not show any polarization sensitivity. CNS2-6 show wavelength dependent polarization sensitivity with 1000 nm showing the highest dichroism. The elliptical lobes in CNS6 could indicate the simultaneous presence of linear and circular dichroism.*

ORD measurements in the visible region were performed by passing unpolarized light through a Glan-calcite linear polarizer (Thorlabs GTH10M). The polarized light, on passing through the CNS sample undergoes a rotation of the plane of linear polarized light to various degrees depending on the radius of curvature and the pitch of the CNS samples.

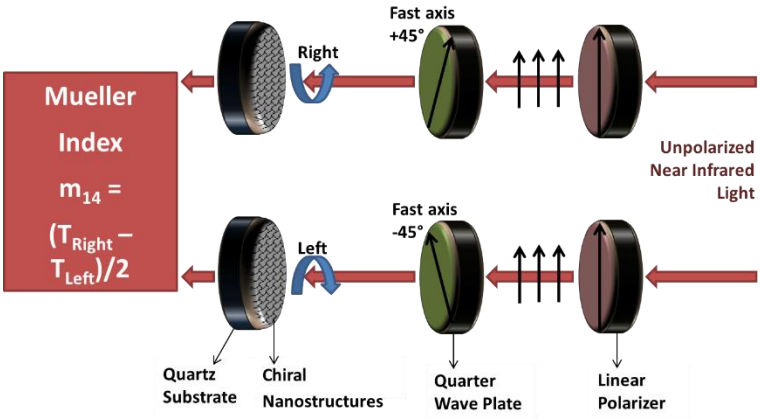

Figure 2.4 *Schematic of the experimental design to determine the Mueller index. The transmittances of the left and right circular polarized light, obtained using the polarizer and quarter wave plate combination, through the sample are determined. The Mueller index can be derived using the formula based on the transmittances.*

The light was then made to pass through an analyzer whose axis was orthogonal to the polarizer. The angle by which the analyzer had to be rotated to achieve a transmission minimum determined the optical activity of the CNS sample. An Ocean Optics (USB4000) and a Bruker Vertex 70 FTIR spectrometers are used to simultaneously obtain the minimum angles of rotation as a function of wavelength over the entire visible and NIR ranges.

2.3 Results and discussion

Circular dichroism was studied in these samples by employing transmission ellipsometry in the visible region and Fourier Transform Infrared (FTIR) spectroscopy in the near infrared (NIR) region. The transmittances of the CNS samples are determined for right and left circular polarized light separately for the NIR region. The Mueller index (m_{14}) can be measured directly using ellipsometry, and it can also be extracted from the FTIR measurements (figure 2.5) using the formula $m_{14} = (T_{right} - T_{left})/2$, where, T_{right} and T_{left} are the transmittances of right and left circular polarized light respectively through the CNS samples (figure 2.5). Note that both ellipsometry and FTIR measurements only measure transmitted light, and therefore, light that is

either absorbed or scattered does not contribute to the m_{14} spectra. The Mueller indices in the NIR region required individual DC offsets to match the visible data. The inset in figure 2.5 shows the first derivative of m_{14} for samples CNS 3 and CNS 6 as examples where there is a smooth overlap between the visible and NIR regions without the need for offseting indicating the DC nature of the offset.

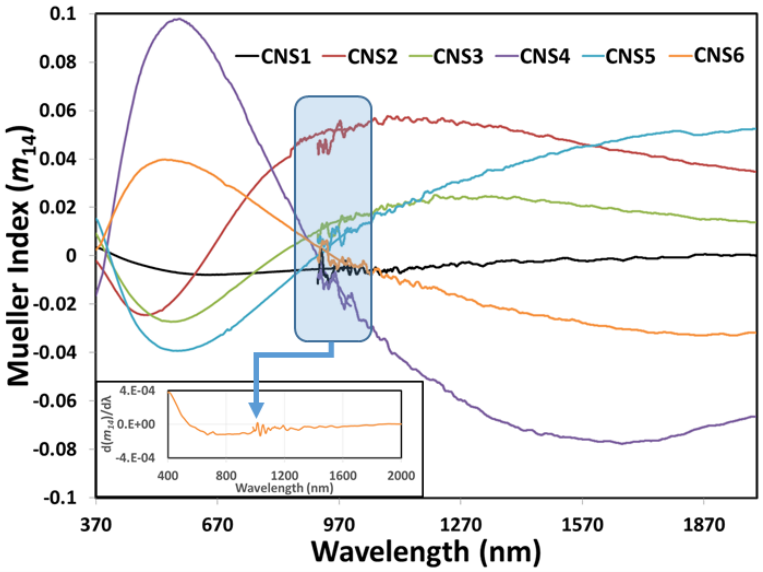

Figure 2.5 *Mueller index extracted from ellipsometry (visible) and FTIR (NIR) transmittances for CNS samples. The samples show a bisignate response with CNS 4 showing the highest circular dichroism at ~570 nm. The rectangular box indicates the overlapping wavelength ranges. The NIR responses were individually offset by adding a DC value to merge with the visible responses. The inset shows the first derivative of the Mueller index for sample CNS6 indicating a good overlap of the visible and NIR regions without the need for offsetting, thus confirming the DC nature of the offset.*

The Mueller index (m_{14}) spectra are directly related to the circular dichroism spectra of the CNS samples, and it can be seen that the samples exhibit selective transmittance of circular polarized light over the entire measured region with a high degree of selectivity. The left or right handedness of the spectra alternate with the different substrate rotation directions of CNS 1 – 6, as would be expected, and the relative optical chirality scales with the chirality of the structure; *i.e.*, the post-like structures have much smaller circular polarization effects than the full and partial

helices. In general, all of the spectra have a broad, bisignate response, where one peak is centered over the visible region and the other opposite peak is centered over the NIR. The visible and NIR peaks have roughly the same intensity in all CNS samples, but the NIR peak does red-shift more strongly than the visible peak for CNS samples with increasing radii of curvature. The most remarkable features of the spectra are the broad m_{14} peaks which are relatively flat over several hundred nanometers in the NIR range, making these films interesting candidates for optical components in that important wavelength region. Larsen et al. describe[41] a computational finite-difference-time-domain (FDTD) model that captures this broadband optical response of the GLAD helical films. The model assumes that individual helices will couple with the incident light through plasmonic resonances, and the polarization sensitivity and energy at which these resonance occurs depends on their morphology.[43,44] In general, the circular polarization sensitive resonances of the helices are similar to standing waves, where the lowest energy mode has zero nodes. The number of nodes increases in integer steps as the excitation energy of the resonances increases. As described above, the morphological parameters of the GLAD films are statistically variable, and therefore, the measured optical response of the film is actually an average response of slightly differently shaped chiral nanostructures. By using FDTD to simulate the individual chiral optical responses of helices having different parameters and then averaging these responses, the computational model was able to capture the broadband chiral optical signature of the GLAD helical films. In particular, the model averaged over the pitch number parameter because this parameter best captures the competitive mechanism of GLAD growth.

Since the CNS samples exhibit significant circular dichroism as described above, it indicates that the samples are also capable of rotating the plane of linear polarized light passing through them. In fact, the circular dichroism and optical rotation dispersion are related through the

Kramers-Kronig relations[45]. To investigate the optical activity of the samples, an experiment was designed which is akin to a polarimeter setup with a slight modification to determine the angle of rotation (figure 2.6). Optical rotation dispersion is obtained by determining the minimum angle by which the CNS samples have to be rotated to obtain minimum transmission in the closed polariscope setup.

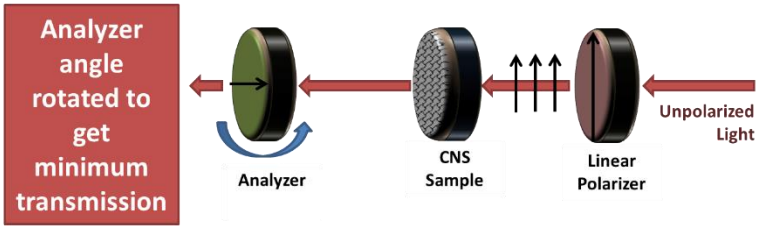

Figure 2.6 *Experimental schematic to determine the angle of rotation of the linear polarization plane by the CNS samples. The sample is placed in a closed polariscope. The angle by which the sample has to be rotated to once again obtain minimum transmission indicates its optical activity.*

According to the polarimetry measurements, the sample CNS 2 had the highest rotation angle of all samples at -17^0 at ~620 nm, which is one of the largest optical rotations of linear polarization reported for thin film samples[46]. Since these structures are both chiral and linearly anisotropic, it may not be possible to completely separate the different contributions in the polarimetric measurements. For example, the experimentally determined orientations for linear polarization transmittance minima might actually result from both linear anisotropy and circular anisotropy since linear polarization can be described in a circular basis. However, the effect of linear birefringence property of the sample could be minimized by first rotating the sample with respect to the polarizer to maximize the throughput. This ensured that the polarizer's axis was parallel to the sample's apparent linear polarization axis. The analyzer is then introduced such that its axis is orthogonal to the polarizer's. The optical activity is then obtained by determining the smallest angle of analyzer rotation which will yield minimum throughput.

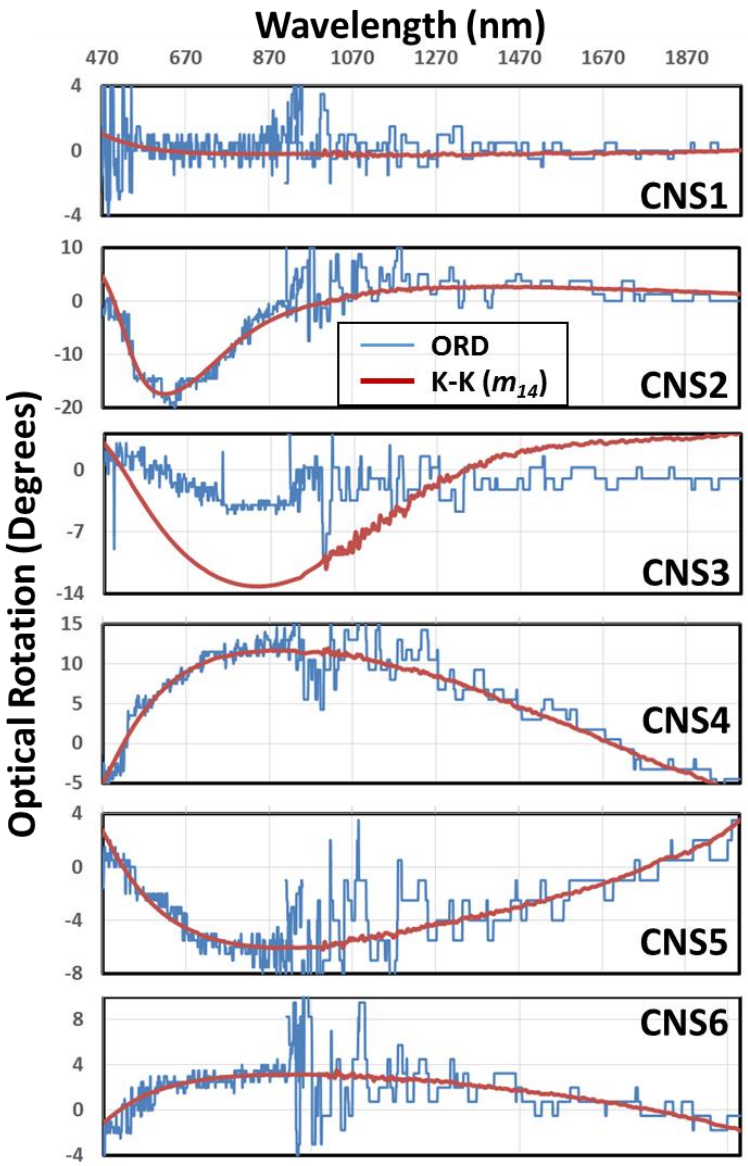

Figure 2.7 *Optical rotation dispersion (ORD) angles as a function of wavelength for CNS samples. The ORD obtained by performing the Kramers Kronig transformation of the Mueller index (m_{14}) extracted from ellipsometry and FTIR spectroscopy is shown in red. Individual DC offsets are done to show the agreement between the optical rotation angles determined from the two experiments. The reason for the deviation of data for CNS3 is not known yet.*

In order to get a different and wider range perspective of the optical rotation of the CNS samples, a numerical Kramers-Kronig (K-K) transformation based on the method by Ohta and Ishida has been applied to CD data obtained from the m_{14} spectra of the CNS samples over the

visible and NIR wavelength regions. The experimentally obtained ORD values conformed well with the ORD obtained from K-K transformed Mueller index in the visible and NIR regions (figure 2.7), except for sample CNS3, the reasons for which are not clear yet. Individual DC offsets are applied to the polarimetric ORD data to show the conformity of the spectra. The good agreement between these spectra is a strong corroboration of the polarimetric experimental design. The results of the K-K transformed Mueller index for the entire visible and NIR region are plotted in figure 2.7**.** While an exact K-K transformation would require integration of all wavelengths and there appears to be some artifacts near the spectral endpoints, the obtained optical rotation spectra are consistent with what would be expected from the m_{14} measurements. That is, the mostly achiral film, CNS 1, does not exhibit significant optical rotation, and the opposite-handed films rotate linearly polarized light in opposite directions. According to the K-K transformations, CNS 2, which is the full helical structure, rotates light the most strongly of the CNS samples, with a large rotation angle of approximately -17° at ~620 nm. In general, optical rotation spectra of the CNS films contain multiple peaks, with the peaks centered at wavelengths <1000 nm rotating light more strongly than the longer wavelength peaks. Another interesting result is that for the one turn helix ($N \approx 1$, CNS 2) and partial helices (pitch number, $N < 1$, CNS 3 - 6), the longer wavelength peak broadens as the pitch number decreases. The intensity of this peak also decreases as the pitch number decreases. A similar effect can be seen in the m_{14} spectra (figure 2.4) for the smaller wavelength peak, but the effect is more pronounced in the optical rotation spectra. Thus, for these helices there appears to be an inverse relationship between the width and intensity of optical rotation peaks.

Far field reflection measurements were performed on samples CNS1 and CNS5 using a Bruker Vertex 70 Fourier Transform Infrared (FTIR) spectrometer in the mid infrared region (1.5 to 25

μm). Polarized light was made to reflect off the samples at a near normal condition. The sample is placed face down (figure 2.8, inset) such that the light first is incident on the nanorods. A 6mm stand-off is introduced between the sample and the reflection stage to protect the integrity of the sample. Figure 2.8 shows the reflection spectra for s- and p-polarization infrared light for samples CNS1 and quartz substrate.

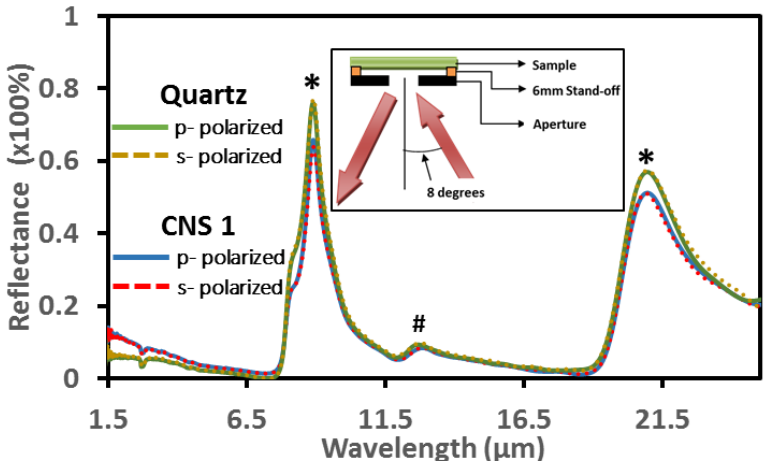

Figure 2.8 *Near normal infrared reflection spectrum of quartz (substrate) and CNS 1 (nanorods on quartz). The vibrational mode (Si-O-Si stretching) and quartz phonon modes are indicated by (#) and (*) respectively. The inset shows the experimental schematic. The reflectance of quartz substrate and CNS 1 are insensitive to polarization.*

The peaks at 8.9 and 21 μm are the phonon modes of the quartz substrate corresponding to Si-O-Si asymmetric stretching and O-Si-O bending modes respectively[47] and the intensities are independent of the polarization. The peak at 12.8 μm is a vibrational mode associated with the symmetric stretching of Si-O-Si bonds[47]. The quartz substrate and CNS1 do not exhibit any changes in reflectance with respect to polarization. The only difference between the quartz substrate and CNS1 is an overall reduction in reflectance. This suggests that, as expected, Ti:Ag nanorods do not have any unique peaks in this infrared region. The reflection measurement was performed on CNS5 sample (figure 2.9). Through the entire mid-infrared region (1.5 to 25 μm), s-polarized reflection spectrum of CNS 5 has similar characteristics to that of quartz substrate.

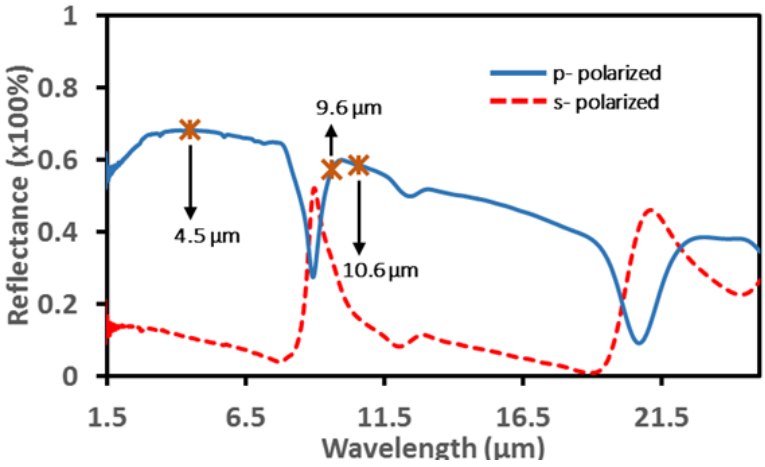

Figure 2.9 *Near normal infrared reflection spectrum of CNS 5 (large radius of curvature). The quartz phonon modes experience a reversal in reflectance with s- and p- polarized light, but the vibrational mode at 12.8 µm remains unchanged. Scattering scanning near field measurements were performed at the wavelengths indicated by (*).*

Broadband polarization sensitivity is observed in the 1.5 to 8 µm region. With p-polarized light the electric field oscillation of the incoming light is along the length of the chiral nanorods and hence experience high reflectance while s-polarized light has low reflectance since it is attenuated with the electric field oscillations being perpendicular to the length of the nanorods. In the quartz reststrahlen region, p-polarized light is expected to have high reflectance since Ag does not have any absorption, however a dip in the reflectance is observed at the quartz phonon mode. There is a reversal in reflectance between s- and p- polarized light at quartz phonon modes (8.9 and 21 µm), but the feature at 12.8 µm due to Si-O-Si symmetric stretching mode does not change although the broadband reflectance (11.4 to 19.3 µm) changes with polarization.

It is known that for a vibrational mode to be polarization infrared active, there has to be a change in the dipole moment. In the case of the symmetric stretching mode at 12.8 µm, there is no effective change in dipole, whereas the modes at 8.9 and 21 µm associated with asymmetric stretching and bending modes have changes in the overall dipole moment hence strongly interacting with polarized infrared light.

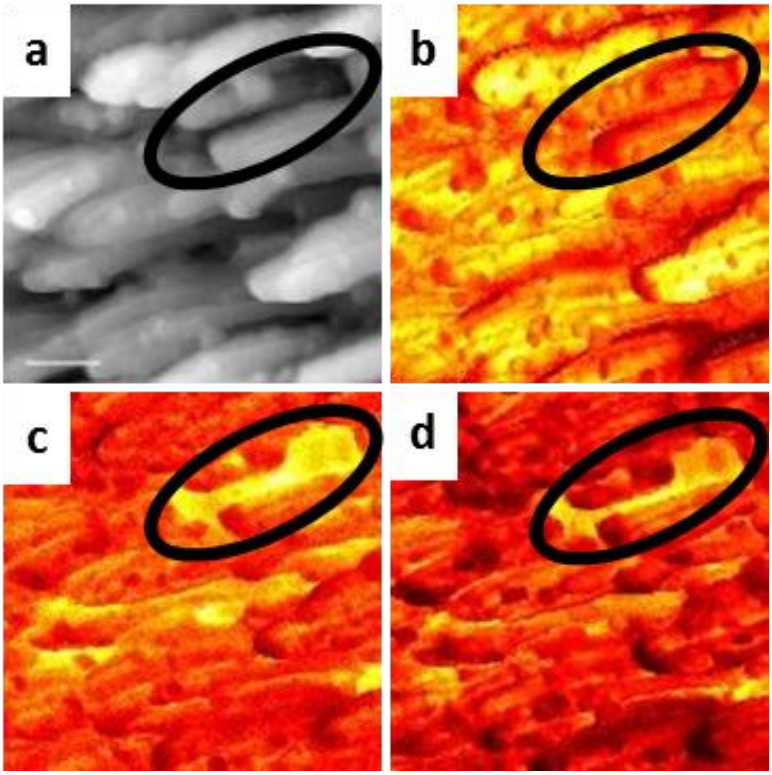

Figure 2.10 *a) AFM image of CNS 5 sample. Scale bar is 200 nm. The oval indicates the area where the substrate (quartz) is visible. Images b, c and d near field plasmonic activity observed at 4.5, 9.6 and 10.6 µm respectively. Near field activity is consistent with the far field reflectance measurement with the highest at 4.5 µm. The activity is reversed in the area indicated by the oval where the substrate is seen.*

With p-polarized light, as expected the overall reflectance is higher, but the dip at the quartz phonon positions are unexpected since as seen in figure 3, quartz should have high reflectance. This suggests that the p-polarized light at these specific frequencies are highly absorbed by the nanorods. But the anomaly is that there is no expected absorption due to silver or due to photonic crystal properties. This suggests that there might exist an interaction between the nanorods and the substrate.

Near field reflection measurements were performed using a scattering Scanning Near field Optical Microscope (s-SNOM) with a tunable quantum cascade laser as the light source. A metallized Atomic Force Microscope (AFM) tip probes the near field properties of the sample by

focusing the infrared beam on the tip thus providing nanometer size resolution. The scattered light carrying the near field information is detected in the far field. The measurements were done using the p-polarized infrared light at the following wavelengths: 4.5, 9.6 and 10.6 μm (indicated in figure 2.9 by *).

Large near field activity is observed on the nanorods at 4.5 μm. However, the area enclosed in the oval (figure 2.10) where quartz substrate is seen with the nanorods absent has no activity. This is reversed when the sample is probed at a wavelength close to the quartz phonon mode (9.6 μm). The near field activity at the quartz area closely follows the far field reflectance observed for quartz substrate (figure 2.8). However, the plasmonic activity on the nanorods diminishes when probed near the phonon mode although the Ag nanorods do not have any absorption features indicating that the light is attenuated by the nanorods. These evidences suggest that there exists a coupling between the plasmons of the Ag nanorods and the phonons of the quartz substrate.

2.4 Conclusion

Chiral nanorods grown using the scalable glancing angle deposition method with self-shadow masking technique were shown to be highly dichroic to circular polarized light with significantly high optical rotation of the plane of linear polarized light, where the specific polarization response could be controlled by the morphological parameters of the thin films. Notably, the observed optical activity of the CNS samples extended over wide regions of the visible and NIR spectrum. The ability to tune the optical activity over the visible and NIR regions by changing the morphological parameters of the CNS samples makes them promising candidates for plasmonic and nanophotonic substrates for biomedical and electro-optic device applications. The narroband absorption of the nanorods as a result of a coupling effect with the phonons of the substrate introduces novel applications such as tunable infrared absorbers and filters.

3 OPTICAL PHONON MODES IN INGAN/GAN DOT-IN-A-WIRE HETEROSTRUCTURES GROWN BY MOLECULAR BEAM EPITAXY

Studies of optical phonon modes in nearly defect-free GaN nanowires embedded with intrinsic InGaN quantum dots by using oblique angle transmission infrared spectroscopy is described here. These phonon modes are dependent on the nanowire fill-factor, doping densities of the nanowires and the presence of InGaN dots. These factors can be applied for potential phonon based photodetectors whose spectral responses can be tailored by varying a combination of these three parameters. The optical anisotropy along the growth (*c*-) axis of the GaN nanowire contributes to the polarization agility of such potential photodetectors.

3.1 Introduction

InGaN/GaN dot-in-a-wire nanostructures have received increasing attention in the past few years due to the pressing need for visible light emitting diodes with high internal quantum efficiency[48,49]. Improved technologies in the growth and fabrication processes and the ability to tune the optical properties by implementing ternary alloy structures have given impetus to this foray. High performance bias selectable photodetectors based on quantum dots embedded in quantum well (dot-in-a-well) structures have been demonstrated previously[50,51]. In this chapter, the infrared optical properties of these dot-in-a-wire nanostructures to determine their candidacy as infrared photodetectors are discussed.

Vertically aligned InGaN/GaN dot-in-a-wire heterostructures were grown on a semi-insulating Si(111) substrate by radio frequency plasma assisted molecular beam epitaxy (figure 3.1). GaN nanowires of 200 nm are first grown at ~750°C. Nitrogen flow rate of 1 sccm and forward plasma power of ~ 400 W were kept stable during the nanowire growth. The fill factor of the nanowires increases radially from the center to the edge of the wafer as seen in figure 3.2. This

is achieved by introducing a temperature gradient radially decreasing from ~750°C at the wafer center to ~700°C at the edge during the nanowire growth process. The wurtzite structured nanowires have their *c*-axis parallel to the growth direction and perpendicular to the substrate surface.

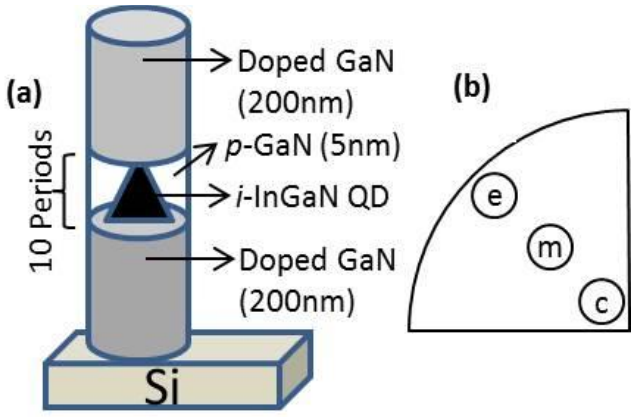

Figure 3.1 *(a) Schematic illustration of a dot-in-a-wire heterostructure on semi-insulating silicon substrate. (b) Schematic of a wafer sector indicating the spots where infrared transmission is done where, 'c' is center, 'm' is middle and 'e' is edge of the wafer. The growth temperature decreases from the center to the edge of the wafer.*

Using a growth technique described elsewhere[49], ten self-assembled intrinsic InGaN quantum dots are then grown at ~600°C and capped by ~5-10 nm GaN layer doped with Mg after each InGaN dot. Approximately 20% indium fraction is attained by appropriately controlling the In and Ga beam fluxes. The indium fraction in the InGaN dot alloy increases from the center to the edge of the wafer inversely proportional to the growth temperature.

The width of the dots varies from 20 to 40 nm and the height varies from 3 to 10 nm. The dots are completely embedded in the center of the nanowires. The nanowire is then capped with another 200nm thick layer of GaN. The doping density estimated from the line width information

from low temperature photoluminescence measurements[52] for this GaN nanowire sample (MN701) is about 10^{18} cm^{-3}.

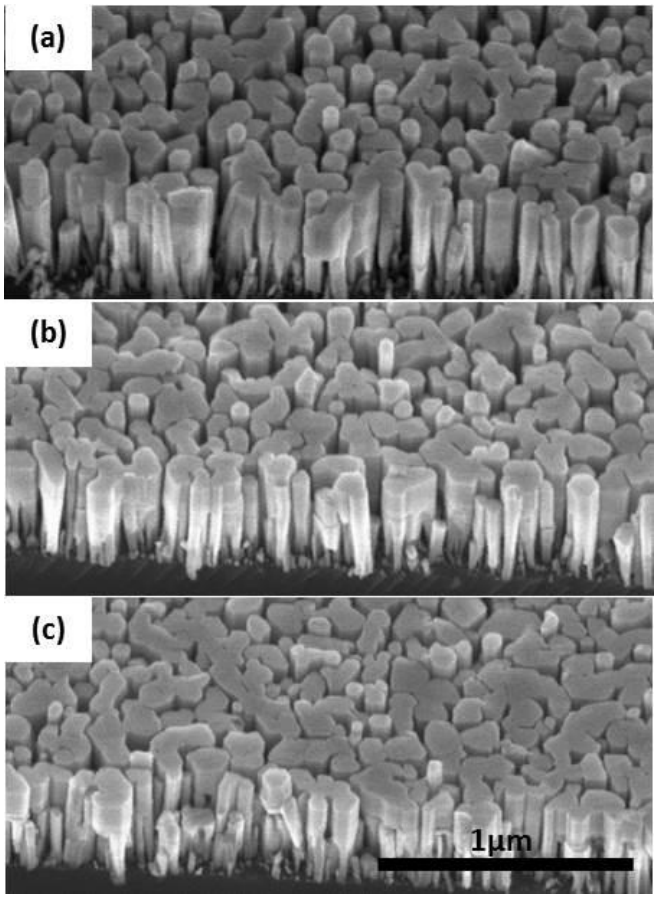

Figure 3.2 *(a) SEM image of a spot at the center of the wafer where the nanowire growth temperature is the highest and hence has the lowest nanowire fill factor. (b) SEM image of a spot at the middle of the wafer. (c) SEM image of a spot at the edge of the wafer where the nanowire growth temperature is the lowest and hence has the highest nanowire fill factor. Estimating from the area under the* E_2 High *TO phonon curve, the middle of the wafer has a filling factor ~1.5 times more than the center and the edge has a filling factor ~5 times more than the center.*

3.2 Experiments and discussions

The sample was optically characterized in the infrared region, specifically the Reststrahlen region of GaN, using FTIR transmission spectroscopy. Measurements were done at the center, middle and edge of the wafer with the edge having a higher nanowire density than the center of the wafer. Owing to the optical anisotropy[53] along the *c*-axis of the nanowires and the fairly

consistent perpendicular orientation of the nanowires to the substrate surface, only transverse optical (TO) phonon modes can be observed with the longitudinal optical (LO) phonon modes almost entirely absent in the normal incidence transmission mode[54]. Characteristic surface optical (SO) modes of nanowires which are longitudinal in nature, are also entirely absent.

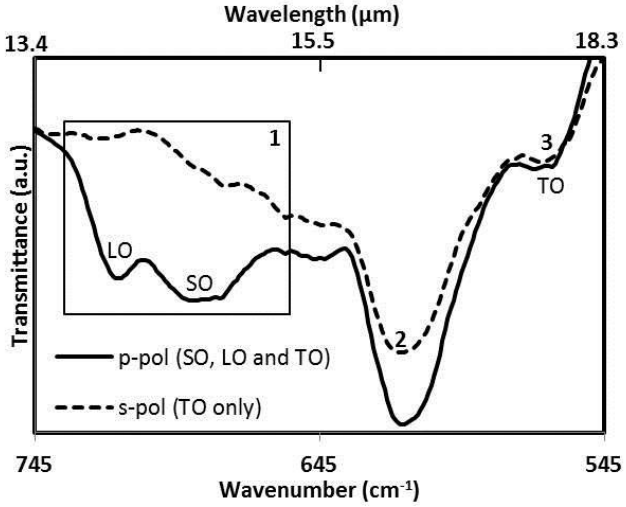

Figure 3.3 *Oblique angle transmittance performed using s- and p-polarized light on a doped (10^{18} cm^{-3}) GaN nanowire with embedded* i-*InGaN QDs (Sample MN701). The s-polarized light does not interact with the* c-*axis of the nanowire hence only TO (3) mode is evident. The electric field component of p-polarized light interacts with the* c-*axis resulting in SO, LO and TO (1,3) modes. The broad transmittance dip at (2) is attributed to the vibrations of hydrogen bonded species[55], C-C phonon and substitutional carbon in the silicon substrate[56].*

In order to study the TO, LO and SO modes, the elegant oblique angle incidence technique[53,57] in the transmission mode was incorporated to exploit the Berreman effect[58]. Employing this technique, s and p polarized lights are made to be incident on the sample at 45 degrees to the normal. With the s-polarized light (TE mode), the electric field component is parallel to the substrate and does not interact with the *c*-axis, hence only the TO mode is observed. But in the case of p-polarized light (TM mode), the electric field component is allowed to interact with the *c*-axis resulting in the observation of both TO and LO modes as shown in figure 3.3. The

observed TO mode at 559 cm^{-1} compares well with other published data for GaN nanowires[59]. However, the broad phonon modes in the sample (~705 cm^{-1}), which are longitudinal in nature do not conform to any previously reported phonon modes for GaN[60-62]. The shift in the peaks toward the lower energy, as the nanowire density decreases, is characteristic of surface optical (SO) modes[62]. It is also observed that the SO mode evolves to the lower energy as the doping density of the nanowire is increased.

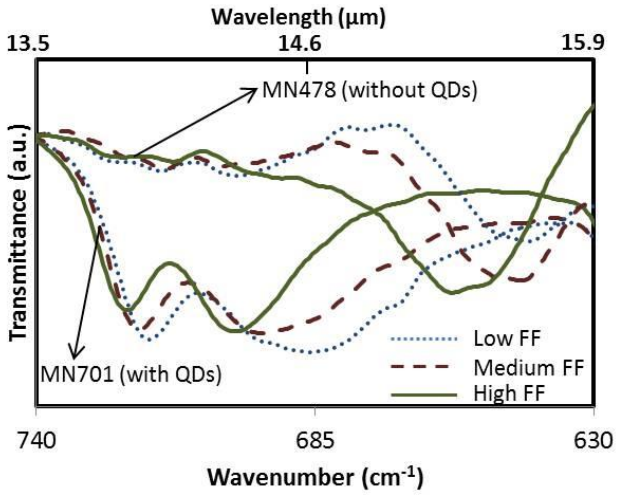

Figure 3.4 *An oblique angle transmission measurement done with p-polarized light. The suspected SO mode at ~705 cm^{-1} in sample MN701(with QDs) shifts to lower energies as the fill factor (FF) decreases. An LO mode is seen at ~722 cm^{-1}. The same measurement done on sample MN478 (undoped GaN without QDs) also indicates a shift of the SO mode (~650 cm^{-1}) to lower energies with decreasing fill factor, but no LO mode is seen indicating that the LO mode in MN701 is indeed due to the* i-*InGaN QDs.*

To understand the possible contribution of the InGaN dot to this anomalous phonon, the same measurements were conducted on a similar intrinsic GaN nanowire sample (MN478) but without the quantum dots. In addition to the (E_1)TO mode, similar SO modes were observed at ~650 cm^{-1}, which is also consistent with previously reported SO mode frequencies for GaN nanowires[60] as shown in figure 3.4. This indicates that the shifted position of the SO modes in the sample (MN701) observed at the three spots on the wafer are due to the presence of the InGaN quantum dots embedded in the GaN nanowires which changes the dynamics of the surface lattice

vibrations. In the doped sample (MN701), as the nanowire packing density is increased by moving the interrogation spot from the center to the edge of the wafer, the SO modes evolve to the lower energy revealing a second peak which was eclipsed by the SO modes at lower nanowire density.

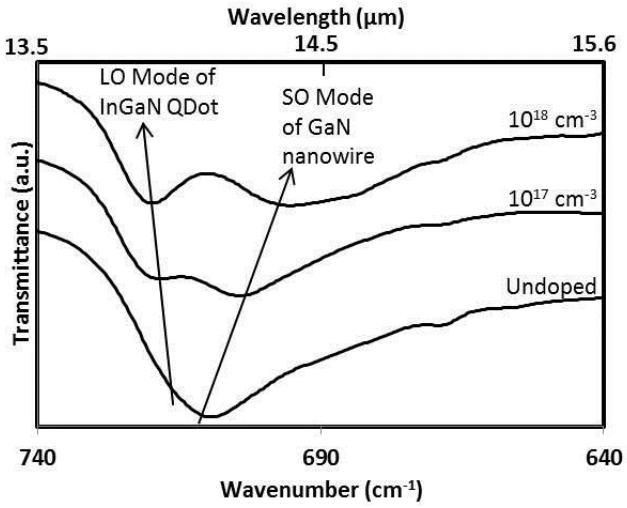

Figure 3.5 *Oblique angle measurement done on GaN nanowires with p-polarized light at varying doping densities with embedded i-InGaN QDs indicating a lower energy shift of the SO mode and a higher energy shift of the QD LO mode with increasing doping densities. In the undoped GaN nanowire sample, the LO mode of the QDs is eclipsed by the SO modes of the nanowires.*

This second peak is identified as LO phonon originating from the InGaN quantum dot. Further, considering the 20% indium fraction, the position of the LO peak is compatible with other published data[63]. The shifting of the LO mode of InGaN to the higher energy as the growth temperature is decreased from center to the edge of the wafer, is due to the increasing indium fraction in the dots as a function of the temperature.

In order to ensure that these shifts are not due to LO phonon modes coupling with the plasmon wave, oblique angle transmission measurements at lower temperatures (250 to 20K) were conducted by mounting the sample in a closed cycle refrigerated cold finger. The observed shift in the LO phonon was only about a couple of cm^{-1} wavenumbers hence ruling out the possibility

of them having phonon-plasmon coupled origin. The observed shift in the position is more likely due to the radial breathing of the nanowires. Figure 3.5 shows the shifting of the LO mode arising from the InGaN dots shifting to the higher energy with higher doping densities. However, the full width at half maximum of the LO phonons remain constant which should not be the case of LO mode coupled with plasmon[64] which again verifies the absence of phonon-plasmon coupling.

Due to the polarization sensitivity of the SO phonon modes, a high extinction ratio up to 72% between the s and p polarized light was observed at oblique angle incidence. This would allow for the design of polarization sensitive infrared photodetectors.

3.3 Conclusion

In summary, this chapter details the observance of surface optical modes by employing the oblique angle incidence technique, in InGaN/GaN dot-in-a-wire heterostructures whose positions are tunable by varying the nanowire density, the indium fraction of the dots and the doping density of the nanowire. Moreover, the anisotropic nature of the *c*-axis of GaN offers polarization sensitivity. These properties of the dot-in-a-wire heterostructures make them a good candidate for phonon based infrared photodetectors.

4 EARLY DETECTION OF CELL ACTIVATION EVENTS BY MEANS OF ATTENUATED TOTAL REFLECTION FOURIER TRANSFORM INFRARED SPECTROSCOPY

Activation of Jurkat T-cells in culture following treatment with anti-CD3 (Cluster of Differentiation 3) antibody is detectable by interrogating the treated T-cells using the Attenuated Total Reflection - Fourier Transform Infrared (ATR-FTIR) Spectroscopy technique. Cell activation was detected within 75 minutes after the cells encountered specific immunoglobulin molecules. Spectral markers noted following ligation of the CD3 receptor with anti CD3 antibody provides proof-of-concept that ATR-FTIR spectroscopy is a sensitive measure of molecular events subsequent to cells interacting with anti-CD3 Immunoglobulin G (IgG). The resultant ligation of the CD3 receptor results in the initiation of well defined, specific signaling pathways that parallel the measurable molecular events detected using ATR-FTIR. Paired t-test with post-hoc Bonferroni corrections for multiple comparisons has resulted in the identification of statistically significant spectral markers ($p<0.02$) at 1367 and 1358 cm^{-1}. Together, these data demonstrate that early treatment-specific cellular events can be measured by ATR-FTIR and that this technique can be used to identify specific agents via the responses of the cell biosensor at different time points post exposure.

4.1 Introduction

The application of Infrared Spectroscopy to measure and identify cellular responses has numerous benefits[65-67]. Cells in culture mount stimulus-specific responses that are induced by receptor:ligand interactions. Here it is hypothesized that ATR-FTIR[68] can be used to identify ligands, e.g., antibodies, pathogens, allergens, molecules, that interact with cells in culture initially via cell surface receptors. The cell under these conditions serves as a ‘sensor’[69] of the

surrounding microenvironment. The identification of the ligand(s) is accomplished by analysis of the resultant ATR-FTIR read-out of ligand-induced perturbations in the cell 'sensor', which initiate intracellular signaling pathways activated as a result of the cell:ligand interactions. Ligands can also be viruses as these interact with specific receptors on the surfaces of cells resulting in types of cytopathic changes over time. These changes have been used historically to identify the presence of viruses in clinical samples, but days and even weeks are sometimes required. Confirmatory assays for specific pathogen identification currently depend on complex molecular methods and the use of defined biological and chemical probes. These assays are generally elaborate, and require specific reagents as well as highly trained technologists and considerable time ranging from three hours[70] to weeks where there is sufficient material for detection. On the other hand, cellular responses become engaged immediately after a cell detects a foreign agent, a stimulant, an antibody, or a pathogen. Learning how to interrogate cells exposed to foreign agents can provide a rapid and sensitive means to identify agents, circumventing the need for more time consuming, technologically complex testing. ATR-FTIR, one mechanism by which cells can be interrogated, greatly reduces background noise, and is more sensitive to the events occurring on the cell membrane compared to transmission FTIR.

4.2 Experimental details

The ATR-FTIR configuration produces enhanced resolution of spectral features[71]. This is confirmed by the features seen in figure 4.1, inset b, where more details with greater signal-to-noise ratios are visible in the ATR-FTIR absorbance curve compared to the FTIR absorbance curve. The use of Fourier Transform Infrared Spectroscopy (FTIR) is reported, employing the Attenuated Total Reflectance (ATR) technique to detect early activation events in Jurkat T-cells after ligation of cell surface CD3-receptors by a specific antibody (anti-CD3) at 75 minutes post

treatment. These findings serve as proof-of-concept that cells in culture can be used as sensors to specifically and rapidly probe the surrounding microenvironment.

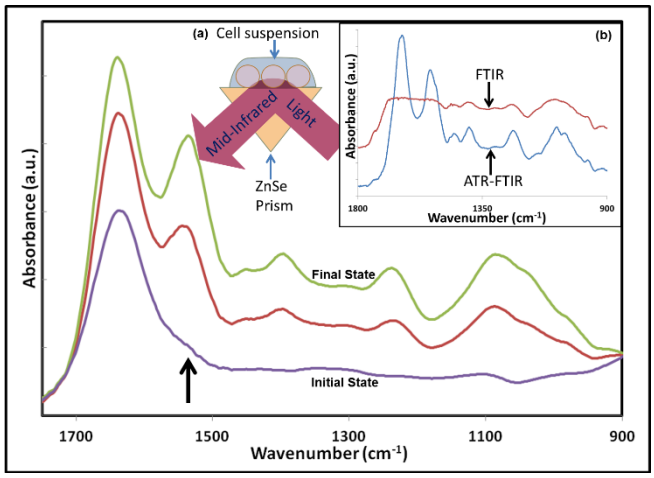

Figure 4.1 *ATR-FTIR spectra of Jurkat cells in culture medium initially showing the characteristic peaks of the medium and ~15 minutes later the peaks representative of the Jurkat cells along with the medium. E.g., the arrow indicates the frequency at which the absorption corresponding to Amide II occurs, which is characteristic of cells as they settle. Inset (a) is a schematic of the ATR technique where a mid-infrared light beam passes through a Zinc Selenide (ZnSe) crystal such that it is totally internally reflected creating an evanescent wave penetrating ~ two microns into the cell suspension deposited on the ZnSe crystal. The light is absorbed by the cell suspension as dictated by the vibrational modes of the components. (The penetration depth and size of the cells are enlarged for clarity) Inset (b) shows the spectra obtained by the conventional transmission mode FTIR and the ATR-FTIR spectroscopy. The ATR-FTIR spectra shows higher signal to noise ratio and better resolved peaks than observed with transmission FTIR alone because the interrogating light penetrates only about two microns into the cell suspension rather than the entire thickness of the cell suspension spot as in transmission FTIR.*

These sensors generate specific spectral patterns resulting from activation of signaling pathways that can serve to identify the specific ligand:receptor interactions which result in a series of intracellular activities over time. ATR-FTIR can interrogate these cells at time points as early as five minutes post exposure/stimulation, or approximately the time it takes the cells to settle onto the crystal surface. When electromagnetic radiation passes through a material, photons of certain frequencies of light, whose energies correspond to the vibrational frequencies of atomic and

molecular bonds are absorbed. ATR is a particular configuration where light is totally internally reflected inside a prism of high refractive index (figure 4.1, Inset a). Some photons penetrate out of the surface of the crystal, and then are coupled back in. This evanescent wave interacts with any material on the surface of the crystal and thus the intensities of the frequencies of light measured after passing through the prism are highly sensitive to the materials present on the surface of the crystal.

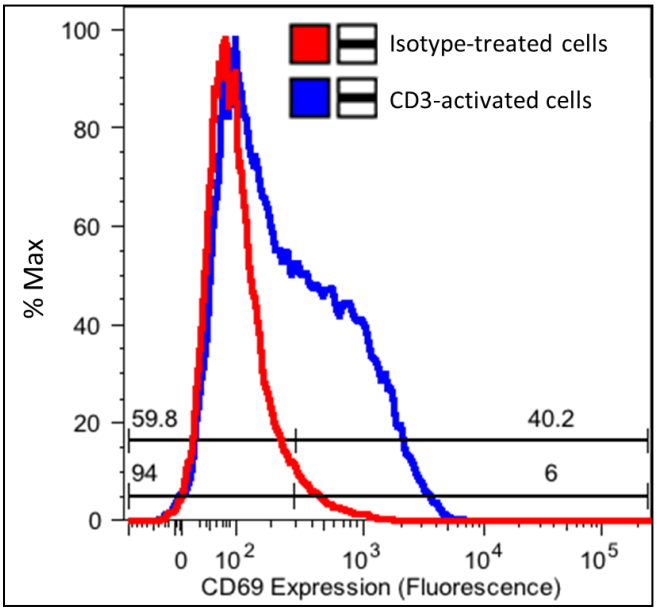

Figure 4.2 *CD69 expression 1 day post activation in CD3-activated Jurkat cells compared to an antibody isotype treated control. This is representative of flow cytometric confirmation of cell activation in our experimental set up that repeatedly yielded > 30% increase in CD69 expression after 24 hours.*

Jurkat T-cells[72] were chosen as model biosensors to be interrogated using the ATR-FTIR spectroscopic technique. Jurkat cells, clone E6-1 (ATCC # TIB-152) were grown in log-phase in R-10 growth medium (RPMI-1640, (Mediatech Manassas, VA); supplemented with 10% fetal bovine serum (FBS), 100 U/ml penicillin, and 100 µg/ml streptomycin). Cells were counted and checked for viability by the trypan blue exclusion method and only cells with >95% viability were

accepted as sensors. The cells were then aliquoted into approximately one million cells each in sterile capped 1.5 ml vials, and centrifuged at room temperature for four minutes at 800g. The growth medium was then completely removed and replaced with 100 µl of either fresh R-10, a matched isotype control antibody, or with R-10 supplemented with 100 ng/ml anti-CD3 IgG (Mabtech, Nacka Strand, Sweden). Cells were gently mixed and incubated in a humidified chamber at 37°C in 5% CO_2 for 75 minutes with the vial lids loosened to allow for gas exchange. At the end of the incubation, the contents of two vials with the same treatment conditions were then pooled together (two million cells per vial). Ice-cold unsupplemented RPMI-1640 medium (1 ml) was added to each vial, which was then centrifuged at 800g for four minutes at room temperature. The supernatant was removed and the pellet washed a second time with one ml of ice-cold unsupplemented RPMI-1640 medium after which the supernatant was removed completely. The pellet of two million cells was re-suspended in 16 µl of cold, fresh, unsupplemented RPMI-1640 medium, placed on ice and transported to the FTIR laboratory for ATR/FTIR analysis (~10 minutes).

Jurkat cells without the anti-CD3 IgG treatment or with an equivalent amount of isotype IgG were used as negative controls. The protocol used to prepare jurkat cells for these measurements are outlined in Appendix 2. The activated state of the experimentally treated cells and the unactivated state of the control cells were validated with parallel flow cytometry experiments (figure 4.2) to measure cell surface expression of the activation marker CD69. The presence of this marker was measured at 24 hours post activation by probing the cell surface (30 minutes, on ice) with CD69 (Fluorescein isothiocyanate) FITC-conjugated antibody (BD Biosciences, San Jose CA) per manufacturer instructions and measured on a BD LSR Fortessa flow cytometer (BD BioSciences, San Jose, CA).

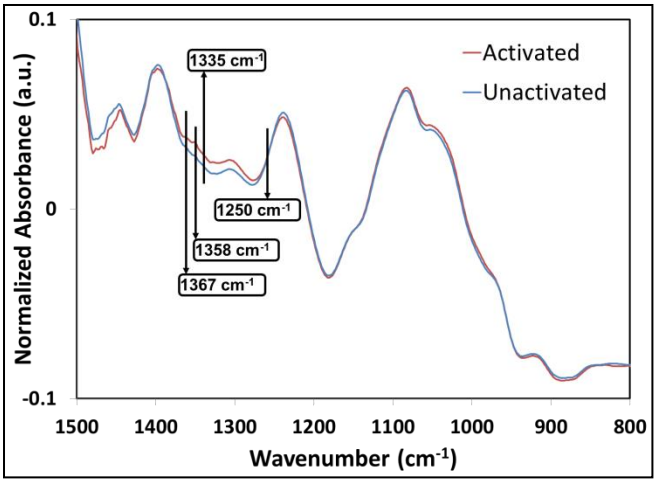

Figure 4.3 *The ATR spectra of the activated and unactivated cells indicating spectral markers with absorbance values that differentiate activated from unactivated cells. The markers are: 1367 cm^{-1}(CH_3- deformation) 1358 cm^{-1} (CH_2-CH rocking), 1335 cm^{-1} (CH_2-CH wagging) and 1250 cm^{-1} (Carbon lattice perturbations, Amide III of proteins).*

For ATR-FTIR analysis, five microliter aliquots of cell suspension (~625,000 cells) were spotted on ZnSe ATR crystal of the Bruker Vertex 70 FTIR spectrometer and allowed to air dry. Spectral data were collected in the range of 1500 to 800 cm^{-1} for the activated and unactivated cells with a spectral resolution of 4 cm^{-1}. As the water evaporated once cells were deposited (~15 minutes), the cells settled to the surface of the crystal and spectral peaks indicative of the biological materials of the cells e.g., proteins, DNA and phospholipids in addition to that of the medium were captured. Each one of the 11 independently prepared activated and unactivated cell sets was scanned by ATR five times consecutively, where each scan consisted of a co-added average of 50 scans.

Sharp spikes due to moisture were evident in the spectral range of 1500-1300 cm^{-1} arising from the standard background subtraction process of the OPUS 6.5 software (Bruker Optics)**.** These spikes were due to the differing moisture levels in the sample chamber during the collection of the background spectrum compared to the sample spectrum resulting in either peaks or dips. These

artifacts were corrected by using an absorbance spectrum of just moisture collected concurrently during sample measurement. The protocol used to correct for the moisture absorbance is detailed in Appendix 1. In later experiments, the moisture noise was further reduced by employing an ATR with dry air purging capability; these experiments also confirmed the tenability of the moisture compensation process. A five point moving average was performed and the spectrum was vector normalized using OPUS 6.5, where the average of all the absorbance values of the spectrum was subtracted from the entire spectrum. This reduced the mid-spectrum to zero. Then the sum of the squares of all the absorbance values was calculated and the spectrum divided by the square root of this sum. The vector normalized ATR spectra revealed some marked differences between the activated and unactivated cells (figure 4.3).

4.3 Results and discussions

Specific frequencies at which the absorbance varied between the activated and the unactivated cells were identified by visual observations. Four spectral frequencies namely, 1358, 1367, 1335 and 1250 cm^{-1} were selected[73] and the differences between the absorbances at these identified frequencies were considered as the differentiating markers. At 1358 cm^{-1} CH_2-CH rocking shifts are measured[74,75]. These shifts are predicted to occur with perturbations to the lipid bilayer comprising the cell membrane. Additionally, protein phosphorylation at specific amino acid residues will alter these bonds. Changes near wavenumber 1367 cm^{-1} arise from deformation[75] of CH_3-, which again reflects membrane changes, likely mirroring events occurring around intracellular membranes, e.g., perturbations in the plasma membranes, nuclear membranes, and endoplasmic reticulum during binding of adapter molecules to the cytoplasmic domain of CD3, resultant signaling, and ultimately nuclear translocation events.

The other significant changes at 1335 cm^{-1} are associated with wagging[74] shifts of CH_2-CH. Such shifts predictably occur with modifications e.g., post-translational modifications, dimerization reflecting protein:protein interactions, while 1250 cm^{-1} measures carbon lattice perturbations[74]. Membrane perturbations will predictably be associated with these events.

Table 4.1 *Paired t-tests on selected spectral bands, corrected for multiple comparisons with false discovery rate analysis.*

Comparisons	**Wavenumber (cm^{-1})**	**Paired t-test Significance**	**Post-hoc Bonferroni Correction**	**Statistically Significant?**
1	1358	0.020	0.050	Yes
2	1367	0.020	0.025	Yes
3	1335	0.028	0.017	No
4	1250	0.038	0.013	No

The null hypothesis states that there will be no difference in the ATR spectrum of Jurkat cells as a function of their state of activation: stimulated with anti-CD3 antibody versus unstimulated. The alternative hypothesis states that there will be differences in the ATR spectrum as a function of the state of stimulation. The independent or predictor variables were the state of activation and the dependent variables were spectral absorbance values.

A two-tailed paired student's t-test was performed using Microsoft Excel 2010 on the absorbance values at the chosen markers and was followed by post-hoc Bonferroni corrections for multiple comparisons with false discovery rate analysis. A confidence interval of 95% was chosen as a test of significance. Of the four spectral markers (Table 4.1), the differences at 1358 cm^{-1} and 1367 cm^{-1} efficiently distinguished the activated from the unactivated cells at 75 minutes after cell incubation with anti-CD3 antibody in eleven independent experiments with p-values of 0.02. Thus,

the null hypothesis is rejected and the alternate hypothesis is accepted. The markers at 1335 cm^{-1} and 1250 cm^{-1} have p values of 0.028 and 0.038 respectively. ATR-FTIR spectroscopic tool has been effectively used here to rapidly detect Jurkat cells early activation events mediated by exposure of cells to antibody specific to the CD3 T-cell coreceptor. Cells were interrogated 75 minutes post exposure and the ratios of specific absorbance values of the cells were calculated and used to differentiate treatment groups. Since the cell fixation[76] or the suspension of the cell activities is critical during the time between the cell culture and the spectroscopic scanning of the samples, other fixation techniques were also investigated. The commonly used chemical fixatives are formalin[77] and formaldehyde[78]. Physical fixation techniques include flash freezing[79] and icing. The main difference between chemical and physical fixation techniques is that reanimation of the cells is possible in the latter. Chemical fixatives causes crosslinking of proteins leading to a more permanent change in the sample. Unactivated jurkat cells were cultured and fixed using formalin, formaldehyde, flash-freezing (cryogenic) and placed on ice (0°C). The four samples were read using ATR-FTIR spectrometer employing the previously mentioned scanning protocol. The efficacy of the fixation techniques is analyzed considering the spectral range 1800 – 1000 cm^{-1}, while paying closer attention to the range 1400 – 1250 cm^{-1}, as the potential activation detection markers are in this region. All the samples are read before fixation and 90 minutes after to monitor the extent of sample degradation. As seen in figure 4.5, formalin, formaldehyde and flash-freezing fixed samples show dramatic differences 90 minutes after fixation. These changes are primarily linked to cross linking of the proteins as evident in the amide II band absorption reduction.

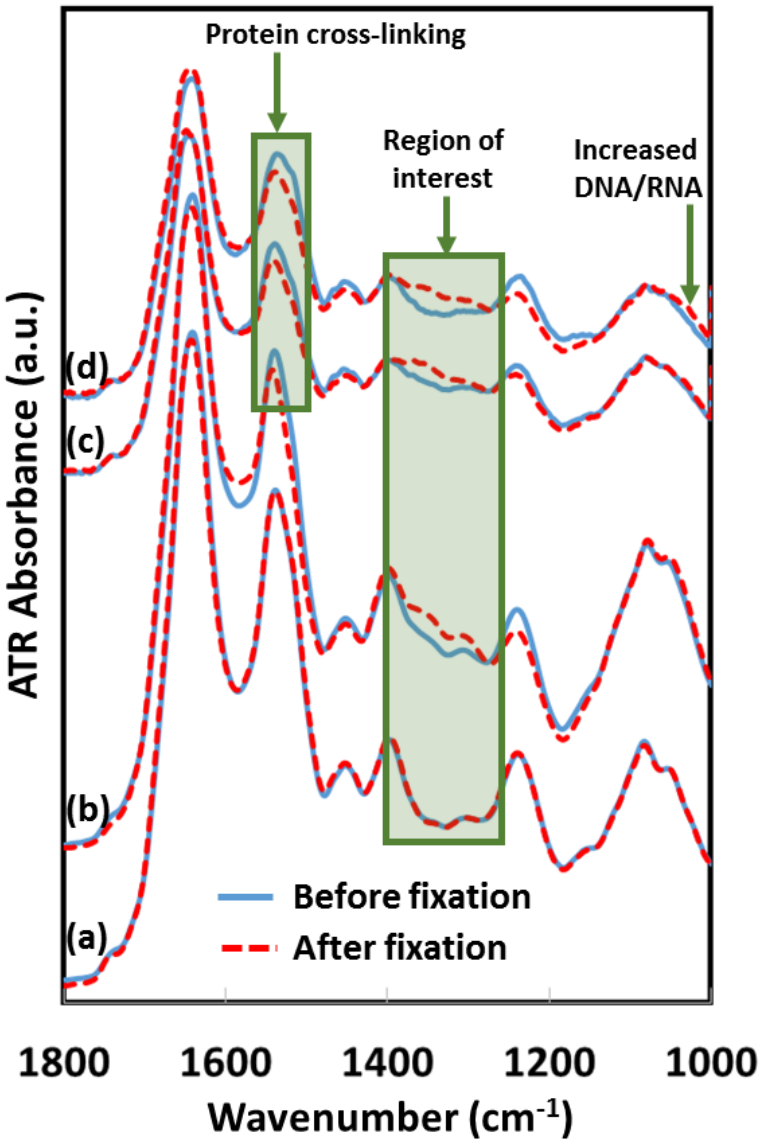

Figure 4.4 *The ATR spectra of the unactivated jurkat cells before and after the following fixation techniques: (a) Sample on ice at 0°C, (b) Flash freezing, (c) Formalin and (d) Formaldehyde. Fixation by placing samples over ice is determined to be the most effective technique as the spectral changes between before and after fixation is the least.*

Moreover, formaldehyde fixed samples show an increase in the DNA/RNA composition as seen in the spectral range of 1150 – 1000 cm^{-1}. This is most likely because of the rupturing of the cell and nuclear membranes due to the sudden variations in the temperature causing the nuclear matter to exit the cell and into the suspension medium. And in all these cases, the cells undergo apoptosis or cell death[80] rendering these fixation techniques unsuitable for infrared

spectroscopic analyses. However, the cells stored over ice at 0°C showed the least spectral changes before and after fixation making it the ideal candidate for suspending cell activity while preserving the morphological integrity of the sample.

Research is currently underway to study the efficacy of using ATR-FTIR spectral markers to identify and differentiate specific agents to which the cells were exposed. In these experiments, the treatment conditions mediating T-cell activation determined by CD 69 cell surface expression has been validated. Figure 4.2 shows a representative output of the validation experiment. An approximate 30% increase in CD69 expression was observed confirming that cells were in fact activated as compared to the isotype treated controls. Ligation of the T-cell receptor, which occurs by treatment of the cells with anti-CD3 activates T cells by modulating specific molecular events including the assembly of specific activation complexes that initiate after the recruitment of the molecule ZAP-70[81,82] (Zeta-chain-associated protein kinase 70) to the cytoplasmic domain of ligated CD3. Ultimately, experimental correlation of the spectral changes with specific activation of signaling events induced by specific agents using more directed approaches will enhance our understanding of the relationship between spectral changes and recruitment of specific molecular interactions.

The spectral changes reported in this work are consistent over numerous experiments, however, the association of these spectral changes with specific molecular events requires additional experimentation to identify whether specific molecular interactions have cause and effect relationships or are simply correlative, non-causal events induced by the cells that are interacting with specific molecules or pathogens, especially because hundreds of genes can be modulated within two hours of early activation events[83]. To identify specific interactions resulting from interactions of cells with agents within the immediate microenvironment, this

experimental model was developed to tightly control the cell membrane and subsequent cytoplasmic events stimulated by the initial interaction, optimizing the technical conditions that enable rapid, efficient, and consistent interrogation of the cell biosensor. The cell as a biosensor responds to cell surface interactions by initiating intracellular signaling pathways that are well defined. These signaling pathways are unique for specific cellular receptors following ligand interaction, e.g.,, the Type-1 interferon receptor ligated to Type 1 interferon or an agonist, which results in intracellular interactions with the cytoplasmic domains of the receptor and Janus kinase (JAK) proteins that are phosphorylated to the cytoplasmic portions of the surface receptor[84,85]. The JAK proteins subsequently recruit STAT-1 (Signal Transducers and Activators of Transcription) proteins, which are phosphorylated subsequently. The series of kinase, phosphate, and protein:protein interactions continue until transcription factors dimerize and translocate to the nucleus[86] to bind to the promoter that drive the genes under the control of the specific receptor that begins the entire sequence of events[87]. ATR-FTIR is then excellent for interrogating modifications and protein interactions occurring in the pathways, along with the protein:DNA interactions, and the subsequent mRNA synthesis[88]. The temporal progression of these events may or not be causal of specific spectral changes measured at the time of ATR-FTIR interrogation, however, these events are occurring and contribute to the overall changes in the cell post exposure. The identified spectral markers will be common only to ligands that interact in precisely the same manner with the CD3 receptor, thus, this technique can be exploited to identify a specific combination of spectral markers at activation time points that are unique to the activating interactions induced by a specific receptor:ligand coupling.

4.4 Conclusion

The utility of using this relatively simple and direct detection of protein modifications, protein:protein interactions, protein:DNA binding, and synthesis of new mRNA transcripts, each resulting in spectral perturbations and the applicability of these measurements to pathogen detection with cells serving as biosensors provides a unique and reliable system for rapid identification of noxious agents and pathogens that threaten health and wellbeing. Cells within organisms are the most sensitive detectors known, far surpassing current technology. Thus, exploiting these as microlaboratories to procure readouts indicative of agents interacting with these sensors has the ability to take detection technologies to the next level.

5 SPECTROSCOPIC SCREENING FOR MEDICAL CONDITIONS

This chapter describes a rapid, simple and cost-effective technique that could lead to a screening method for colitis without the need for biopsies or in vivo measurements. This screening technique includes the testing of serum using Attenuated Total Reflectance Fourier Transform Infrared (ATR-FTIR) spectroscopy for the colitis-induced increased presence of mannose. Chronic (Interleukin 10 knockout) and acute (Dextran Sodium Sulphate-induced) models for colitis are tested using the ATR-FTIR technique. Arthritis (Collagen Antibody Induced Arthritis) and metabolic syndrome (Toll like receptor 5 knockout) models are also tested as controls. The marker identified as mannose uniquely screens and distinguishes the colitic from the non-colitic samples and the controls. The reference or the baseline spectrum could be the pooled and averaged spectra of non-colitic samples or the subject's previous sample spectrum. This shows the potential of having individualized route maps of disease status, leading to personalized diagnosis and drug management.

5.1 Introduction

Inflammatory bowel diseases (IBDs), Crohn's disease and ulcerative colitis, are multifactorial disorders whose etiologies remain obscure. Although the exact pathogenesis is poorly understood, there is evidence that it involves interactions among the immune system, genetic susceptibility, and the environment, most notably the bacterial flora.

The two major forms of IBDs, Ulcerative Colitis[89] and Crohn's disease[90] are debilitating gastrointestinal tract disorders that can lead to life threatening complications such as colorectal cancer[91]. Assessment of intestinal inflammation in IBD remains a difficult challenge[92]. Currently, the clinical diagnosis is achieved by colonoscopy that assesses the endoscopic appearance of the colon. However, this technique is not ideal for monitoring disease

activity regularly or as an annual checkup since it is expensive and invasive, requiring sedation. Thus, there is a need for new, low risk, simple, inexpensive and objective tools for IBD diagnostics.

In the last two decades, Infrared spectroscopy has greatly enhanced clinical medicine through advancements in the field of spectroscopy and imaging. Specifically, there is an emerging infrared technology called Attenuated Total Reflectance Fourier Transform Infrared (ATR-FTIR) spectroscopy used in life sciences. This technique[93] is sensitive to the bond vibrations of the molecular composition of the sample and requires minimal sample preparation[88,94], which provides a rapid diagnostic alternative to biological assays[95].

5.2 Materials and methods

Mice

Three week-old female C57BL/6 wild type (WT) and interleukin 10 knockout (IL10-/-) mice were obtained from Jackson Laboratories (Bar Harbor, ME). Toll-like receptor knockout (TLR5-/-) mice were grown in our facility. Mice were group housed under a controlled temperature (25°C) and photoperiod (12:12-h light–dark cycle) and fed *ad libitum*. All studies were performed in accordance with the Institutional Animal Care and Use Committee at Georgia State University (Atlanta, GA), permit number: A14010.

Development of colitis in IL10-/-

IL10-/- mice develop colitis on a time dependent manner. In order to assess the intestinal inflammation in those mice at different times of colitis development, feces were collected at week 4 and week 14 to measure Lcn-2. Blood was collected at week 4 and 14 to obtain sera by centrifugation using serum separator tubes (BD Biosciences, Franklin Lakes, NJ)

Dextran Sodium Sulphate (DSS) induced Colitis

C57BL/6 WT mice were administered DSS (MP Biomedicals, Solon, OH) at 3% in drinking water ad libitum for 7 days. Feces and blood were collected at day 0 (before DSS treatment) and day 7. Hemolysis-free serum was collected by centrifugation using serum separator tubes. Mice were sacrificed by CO_2 euthanasia.

Collagen Antibody-Induced Arthritis Model

BALB/C WT mice received collagen antibodies injections (200 µL) on day 0 by an intravenous injection (tail vein). On day 6, mice received a lipopolysaccharide (LPS) boost injection (200µL) by intraperitoneal injection. Blood samples were collected from each mouse on pretreatment (day -2) and on day 12 from the jugular vein. Hemolysis-free serum was collected by centrifugation using serum separator tubes.

TLR5-/- model of metabolic syndrome

TLR5-/- spontaneously develop metabolic syndrome as previously described[96]. Age-matched WT and TLR5-/- mice were fasted for 5-h and baseline blood glucose levels measured with a blood glucose meter (Roche) using blood collected from the tail vein.

H&E staining of colonic tissue

Mouse colons were fixed in 10% buffered formalin for 24 hours at room temperature and then embedded in paraffin. Tissues were sectioned at 5-µm thickness and stained with hematoxylin & eosin (H&E) using standard protocols. Images were acquired using a Zeiss Axioskop 2 plus microscope (Carl Zeiss MicroImaging) equipped with an AxioCam MRc5 CCD camera (Carl Zeiss).

Quantification of fecal and serum Lcn-2 by ELISA

Fecal samples were reconstituted in PBS containing 0.1% Tween 20 (100 mg/ml). After centrifugation, clear supernatants were collected. Serum samples were diluted in kit-recommended reagent diluent (1.0% BSA in PBS). Lipocalin-2 (Lcn-2) levels were estimated in the supernatants and/or serum using Duoset murine Lcn-2 ELISA kits (R&D Systems, Minneapolis, MN).

Colonic Myeloperoxidase (MPO) Assay

Neutrophil influx in colon was analyzed as marker of inflammation by assaying the enzymatic activity of MPO, a neutrophils marker. Briefly, tissue (50 mg/mL) was thoroughly washed in PBS and homogenized in 0.5% hexadecyltrimethylammonium bromide (Sigma, St. Louis, MO) in 50 mM PBS, (pH 6.0), freeze-thawed 3 times, sonicated and centrifuged. MPO was assayed in the clear supernatant by adding 1 mg/mL of dianisidine dihydrochloride (Sigma) and 0.0005% H_2O_2 and the change in optical density measured at 450 nm. Human neutrophil MPO (Sigma) was used as standard. One unit of MPO activity was defined as the amount that degraded 1 mmol peroxidase per minute.

Fourier Transform Infrared (FTIR) Spectroscopy

A Bruker Vertex 70 FTIR spectrometer was used to obtain all the spectroscopic results. The samples were scanned covering the wavelength range of 4000 to 400 cm^{-1} and the 1800 to 1000 cm^{-1} section was used for this study. A medium Blackman-Harris appodization was employed with a resolution of 8 cm^{-1}. The samples were scanned 50 times and averaged. Each co-added sample scan was repeated 5 times and averaged. A room temperature Deuterated Lanthanum Alanine doped TriGlycine Sulphate (DLaTGS) pyroelectric detector was employed. The infrared light beam intensity was controlled by passing it through a 3mm aperture. This is done to optimize

the detector response and prevent saturation. A Parker-Balston dry air purging system was used to reduce the moisture and carbon dioxide levels of the ambient air in the spectrometer.

Attenuated Total Reflectance (ATR) configuration

MVP-Pro ATR accessory from Harrick-Scientific was used for all spectroscopic measurements in this study. A diamond crystal (1mm x 1.5mm) was the internal reflection element configured to have a single reflection of the infrared radiation. A sample of one microliter is deposited on the crystal surface and allowed to air dry (~5 minutes). An evanescent wave with an approximate penetration depth of 2 microns (dependent on the refractive indices of the ATR crystal and sample and the wavelength of light) interacts with the sample. The output spectra is an ATR absorbance spectra which is subsequently analysed.

Post processing techniques

The 5 reads of the 50 co-added scans for each sample (total of 250 scans) are averaged. The spectra were sectioned to the 1800 to 1000 cm^{-1} range. Using OPUS 7.2 software, all the spectra were internally normalized[97] by scaling the entire sectioned range so that the absorbance value at the 1642 cm^{-1} peak (Amide I) was 2.0. Spectral deconvolution was also done to better resolve the peaks by obtaining the second derivative followed by a 9 point smoothing using Microsoft Excel software.

Data analysis techniques

Cluster and heterogeneity analyses were carried out in the spectral range of 1140 to 1000 cm^{-1} using the Bruker Optics OPUS 7.2 software. The algorithm calculates the Euclidean distance between each spectrum and groups them into clusters based on the conformity of the spectra with each other. The resulting data is plotted as a heterogeneity dendrogram chart where the heterogeneity index on the y-axis indicates the degree of heterogeneity between the identified

clusters. Student's t-tests were carried out for the DSS study and not for the IL10-/-, CAIA and Metabolic syndrome studies due to the smaller sample sizes, although the uncertainty levels of the averages are shown.

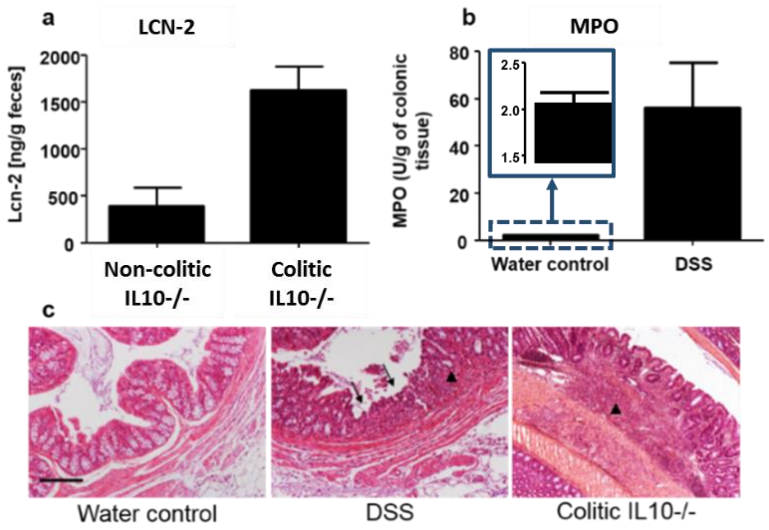

Figure 5.1 *(a) Lcn-2 was quantified in the feces of mice showing a clear increase of Lcn-2 in colitic IL10-/- Vs. non-colitic IL10-/- mice. (b) Colonic Myeloperoxidase (MPO) activity was quantified in the distal colon of DSS induced-colitis compared to water control mice agreeing well with the spectroscopy data. (c) Respective H&E-stained colons of WT water control, DSS-induced colitis and colitic IL10-/- mice indicate sites of lymphocytes infiltrations (arrow heads) and erosion of the crypt figures (arrows). Scale bar: 100µm.*

5.3 Results and discussion

IL10-/- mouse model[98] closely resembles the physiological, histological and biochemical features of human chronic colitis and develops colitis mediated by T helper cell 1 (Th1) cells. Mice with targeted deletion of the IL10 gene spontaneously develop chronic enterocolitis with massive infiltration of lymphocytes, activated macrophages, and neutrophils in a Th1 cell-mediated mechanism[99]. The predictability of the timing of colitis in IL10-/- mice allows longitudinal assessment of blood samples during colitis progression from 4 weeks (no symptoms shown) up to 14 weeks, the age at which the mice display signs of severe colitis. The second model, DSS-induced colitis[100,101] is a commonly used chemically-induced mouse

model of acute colitis which has similarities to ulcerative colitis in human. DSS first disrupts the intestinal barrier functions followed by an increase of inflammation which closely resembles histological and clinical characteristics of IBDs such as ulcerative colitis[102,103].

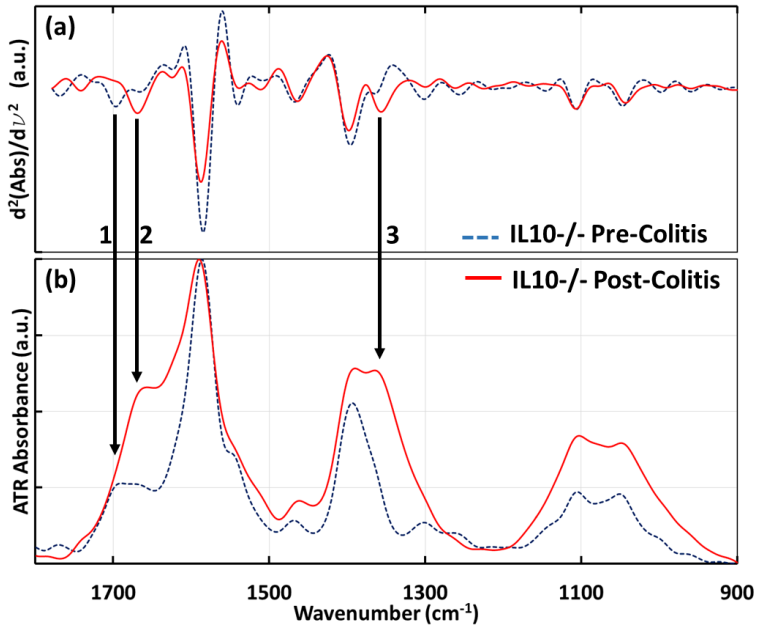

Figure 5.2 *(b) ATR-FTIR absorbance spectra of purified RNA from interleukin 10 knockout mice serum before and after developong colitis. (a) shows the second derivative of the absorbance indicating three clear peaks differentiating post from pre-colitis. The peaks 1, 2 and 3 corresponding to β-sheet folding of Amide I, Guanine and methyl group vibrations respectively, clearly distinguish the post from pre-colitic purified RNA samples.*

To confirm the effectiveness of these two models as tools for investigating spectral markers for colitis, the development of colitis was assessed in these mice using other established techniques. Histological features were assessed by H&E staining, and the degree of inflammation was measured in DSS and IL10-/- model by respectively assessing MPO activity, a marker of inflammation in the colon[104], and measuring fecal Lipocalin 2 (Lcn-2) levels, previously described[105] as being a robust fecal marker that correlates with the severity of inflammation. MPO is produced by neutrophils, a class of leukocytes that highly infiltrate into the mucosa in a situation of intestinal inflammation. Increases of Lcn-2 levels and MPO activity in the feces of

IL10-/- mice (figure 5.1a) and in DSS-induced colitis colon samples (figure 5.1b) respectively, were observed. The increase of lymphocyte infiltration (figure 1c, arrow head) and the erosion (figure 5.1c, arrow) of intestinal glands (crypt), observed on the H&E stained picture of the colon confirmed that, in contrast to the control groups (non-colitic), the DSS-treated and the IL10-/- mice develop colitis.

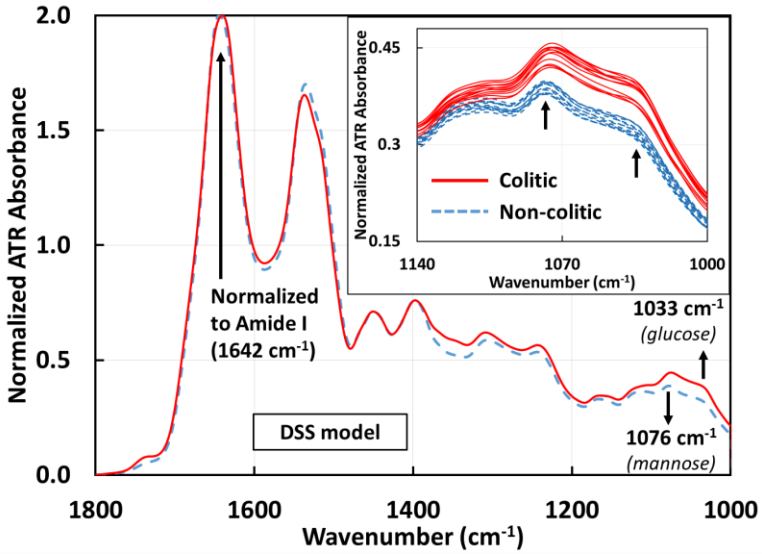

Figure 5.3 *Averaged ATR-FTIR spectra of sera drawn from mice before (n=12) and after (n=12) developing colitis induced by 3% DSS. The differentiating markers 1033 and 1076 cm^{-1} are identified as glucose and mannose with p-values of 4.43E-8 and 7.59E-8 respectively. The inset shows the individual serum samples from 1140 – 1000 cm^{-1} for clarity. Individual colitic and non-colitic spectra show a clear separation between the groups. With further data points it should be possible to find an absorbance range for the two groups. All spectra are normalized to the Amide I peak (1642 cm^{-1}). The averages for the glucose peak are 0.3175±0.0024 (non-colitic) and 0.3788±0.0041 (colitic) and the averages for the mannose peak are 0.3847±0.0022 (non-colitic) and 0.438±0.0035 (colitic).*

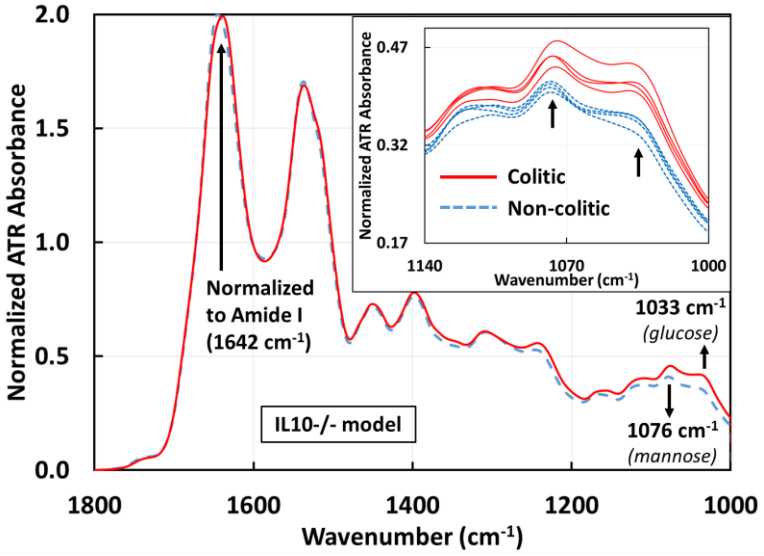

Figure 5.4 *Averaged ATR-FTIR spectra of sera drawn from IL10-/- mice before (n=4) and after (n=4) spontaneously developing colitis. The same markers 1033 and 1076 cm^{-1} identified in the DSS model are effective in differentiating colitic from non-colitic spectra of the IL10-/- model. The inset shows the individual serum samples from 1140 – 1000 cm^{-1} for clarity, again showing a clear separation between the two groups. All spectra are normalized to the Amide I peak (1642 cm^{-1}). The averages for the glucose peak are 0.3491±0.0057 (non-colitic) and 0.412±0.009 (colitic) and the averages for the mannose peak are 0.4071±0.0034 (non-colitic) and 0.4553±0.0081 (colitic).*

Initial spectroscopic measurements (figure 5.2) were performed on purified RNA samples extracted from the serum of IL10-/- mice before and after developing colitis. Figure 5.2b shows clear differences between post and pre-colitic purified RNA samples after normalization to the largest peak. Figure 5.2a shows the second derivative which resolves the peaks that uniquely differentiates identifying them as beta sheet folding of proteins (1), guanine (2) and methyl group vibrations (3). However, the major goal of this project was to be able to see a systemic and global change in the serum that could be used to distinguish diseased and non-diseased state. The key being minimal sample preparation.

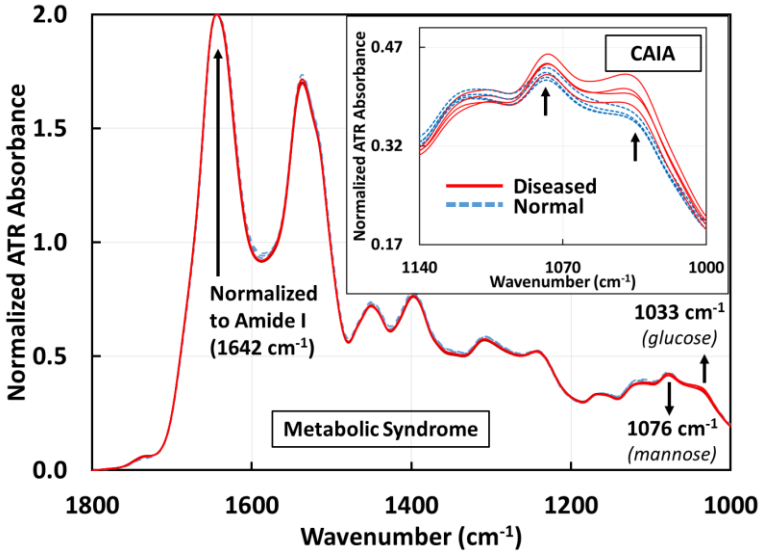

Figure 5.5 *ATR-FTIR spectra of sera drawn from mice before (n=4) and after (n=4) developing metabolic syndrome. In these 8 spectra, the two spectral markers at 1033 cm^{-1} and 1076 cm^{-1} do not show any difference in the metabolic syndrome samples with respect to ATR-FTIR technique. The inset shows the spectra (1140 – 1000 cm^{-1}) of sera drawn from collagen antibody-induced arthritic (n=4) and normal (n=4) mice (total of 8). 1033 cm^{-1} marker is common to colitis and arthritis, but 1076 cm^{-1} marker is unique to colitis. All spectra are normalized to the Amide I peak (1642 cm^{-1}).*

To this end, spectroscopic measurements were performed on sera which is plasma separated from whole blood from DSS-induced colitis mice compared to the same mice before intake of DSS (control mice) and on colitic IL10-/- mice compared to the same mice before the development of colitis. Serum was chosen due to its stability and absence of any additives such as anticoagulants. Serum samples were deposited on the ATR crystal and allowed to dry. By allowing the water in the sera to evaporate, the signal to noise ratio of the spectral signal of other sera components are greatly enhanced, which are otherwise occluded by the broad water absorption. Similar significant differences in absorbance were observed in both DSS (figure 5.3) and IL10-/- (figure 5.4) mouse models between the control groups (non-colitic) and the colitic groups at ~1033 cm^{-1} and ~1076 cm^{-1}. Both absorbance peaks have been attributed to the symmetric stretching

modes of C-O indicating the presence of saccharides[106], with the vibrational modes at ~1033 cm^{-1} and ~1076 cm^{-1} due to glucose and mannose respectively[107].

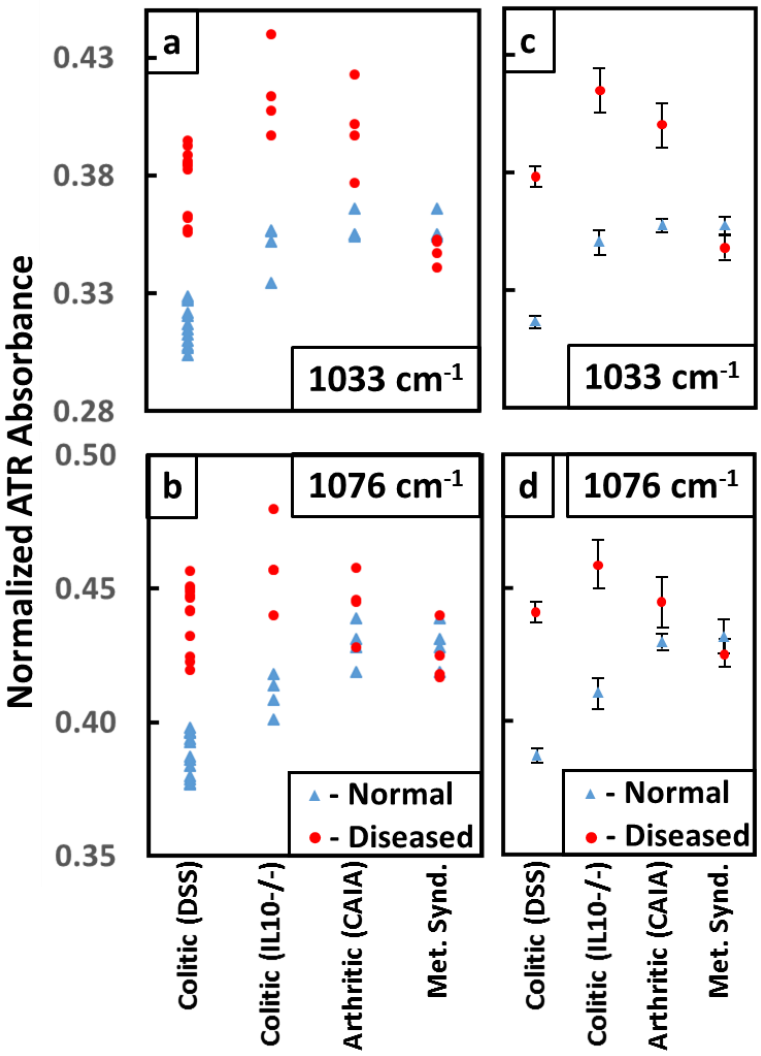

Figure 5.6 *Plot of the absorbances for the glucose peak (a) at ~1033 cm^{-1} and the mannose peak (b) at ~1076 cm^{-1} for Colitic (DSS), Colitic (IL10-/-), Arthritic (CAIA) and Metabolic syndrome samples. (c) and (d) show the average values of absorbances for the normal and diseased samples with the error bars. The error bars associated with the normal samples are much smaller than the diseased samples as expected. The metabolic syndrome samples do not show a separation from the normal at either of the two peaks. However especially for colitis samples, there is a clear separation from the normal samples. The absorbance data associated with the peak at ~1033 cm^{-1} for arthritis also show a separation but not at ~1076 cm^{-1}. Hence this analysis shows that the absorbance data related to the mannose peak at ~1076 cm^{-1} is unique to colitis.*

In order to classify samples as either colitic or non-colitic, machine learning strategy was used. A chemometric model was developed by using 23 out of the 24 non-colitic and DSS-induced colitic samples to calibrate the model.

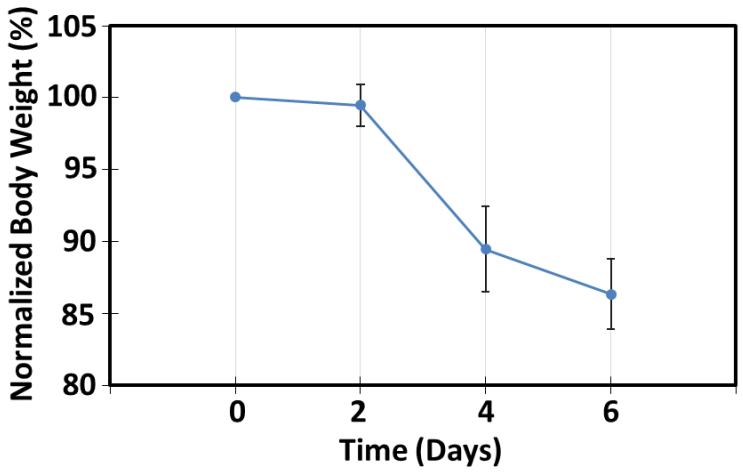

Figure 5.7 *Normalized and averaged body weight of 12 mice developing colitis. The body weight reduced to ~86% indicating severe colitis by day 6 of ingesting 3% DSS in drinking water.*

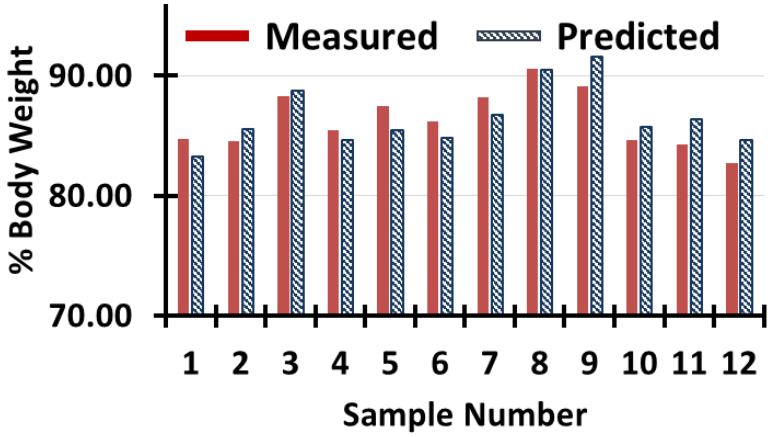

Figure 5.8 *Chemometric projection of the body weight of the mice before and after developing colitis. The correlation between the mannose absorbance levels and the body weight was ~81%.*

The one sample that was excluded at a time was used to validate the model. The calibration and validation is thus cycled through all the 24 samples. This model is called cross validation[108].

This model is best suited for samples of smaller sizes. Colitic mice are shown to reduce in body weight by 10 to 17% beyond which the mice are euthanized. The body weight of the mice for the DSS colitic study were measured (Figure 5.13). The weights were normalized to day 0 being 100%. The average reduction of the body weight by day 6 was ~86% indicating severe development of colitis. The previously identified signature of mannose was used in this chemomteric cross validation method. The absorbance value after performing the appropriate normalization (previously described) is associated with the corresponding colitic or non-colitic normalized body weight. A partial least square regression is performed on the 23 samples which is considered as the calibration set and the excluded sample is used to validate, thereby predicting the body weight of the mouse on day 6 simply by knowing the mannose absorbance level (figure 5.14). The 24 (colitic and non-colitic) samples are cycled through this process. The predicted body weight of the mice had a correlation factor of ~ 81% when compared with the mannose absorbance levels. This machine learning process can be translated to other assays such as myeloperoxidase or lipocalin-2 protein levels.

It has been reported that in colitis serum samples, there is a reduction in butyrate oxidation with a compensatory increase in the oxidation levels of glucose[109]. Hence, the increase in the absorbance at ~1033 cm^{-1} in colitic serum samples could be an indication of colitis. Studies in humans have shown the co-occurrence of ulcerative colitis with that of diabetes and glucose intolerance[110]. In order to exclude the possibility that the mannose and glucose peaks obtained for the IL10-/- and DSS-induced models of colitis originate from the co-occurrence of other glucose intolerance conditions, similar assays were performed using a mouse model developing metabolic syndrome.

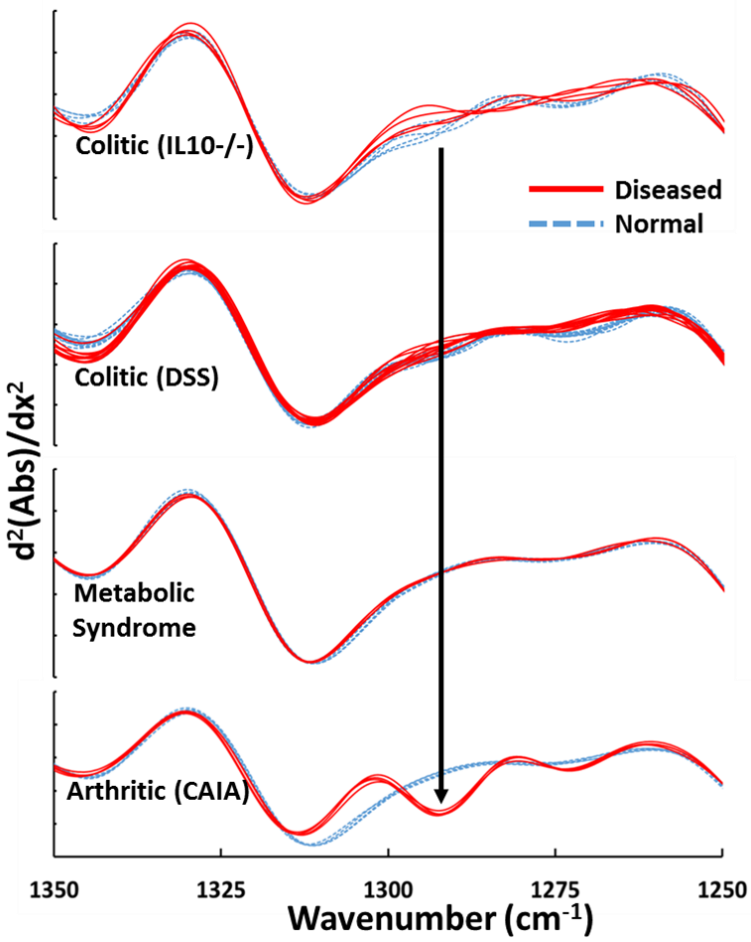

Figure 5.9 *Second derivative of the absorbances of colitic (IL10-/- and DSS), metabolic syndrome and arthritic samples clearly indicating the 1292 cm^{-1} peak identified as thymine which is unique to arthritis.*

Mice deficient of Toll-like receptor 5, a component of the innate immune system that is expressed in the intestinal mucosa, exhibit hyperphagia and develop the hallmark features of metabolic syndrome, including hyperlipidemia, hypertension, insulin resistance, and increased adiposity [111]. As seen in figure 5.5, metabolic syndrome samples did not show any significant differences in absorbance at the ~1033 cm^{-1} and ~1076 cm^{-1} peaks with respect to ATR-FTIR spectroscopy in this wavelength range of interest. This indicates that these particular mannose and glucose peaks observed in colitic samples were not a result of metabolic syndrome.

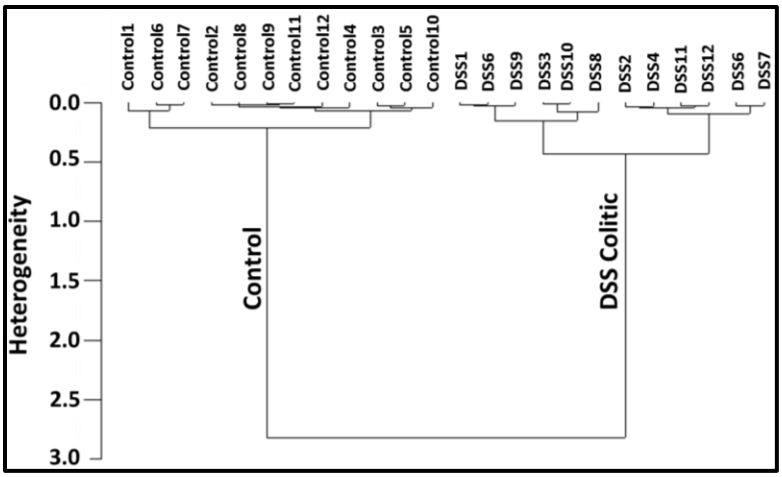

Figure 5.10 *Dendrogram plots of the cluster analyses of colitis DSS sample spectra (12 colitic and 12 control) in the range of 1140 to 1000 cm^{-1} to include glucose (1033 cm^{-1}) and mannose (1076 cm^{-1}) peaks. The spectra are correctly classified into the colitic and control groups based on their conformity to each other. Large heterogeneity is seen between colitis and control samples (2.5) indicating that the two groups are distinctly different. Similar heterogeneity (1.3) is seen in the IL10-/- study.*

The next objective was to determine whether the absorbance changes in the two peaks at ~1033 cm^{-1} and ~1076 cm^{-1}, were specific to intestinal inflammation or associated with any kind of inflammation. Collagen antibody-induced arthritis (CAIA) was employed as a model of extra-intestinal inflammation. An increase in absorbance was seen in arthritic sera samples at ~1033 cm^{-1} (similar to colitic samples), but not at ~1076 cm^{-1} as previously seen in the inset of figure 5.5. This result suggests that the glucose peak might not be specific to colitis but general to an inflammation from any origin. However, the mannose peak at ~1076 cm^{-1} appeared to be specific to colitis. It has been reported that in ulcerative colitis cases in humans, one of the glycoprotein fractions in the colonic mucus has elevated levels of mannose that was confirmed using biological assays[112]. The lesions on the colon characteristic of colitis can facilitate the diffusion of mannose into the circulating blood stream, thus manifesting as increased levels of mannose in serum[113]. This phenomenon could explain the increased levels of mannose in the colitic mice

serum samples in the DSS model at ~1076 cm^{-1} spectral marker. Another study using Proton Nuclear Magnetic Resonance spectroscopy reports that there is a significant increase in mannose levels[114] in the serum for DSS-induced colitic mice which is confirmed by our ATR-FTIR spectroscopic study.

As seen in figure 5.6a, the absorbance levels at ~1033 cm^{-1} indicated that the glucose peak increased at the onset of arthritis and colitis. The absorbance data points for the metabolic samples did not show a clear separation from the normal in either individual (figures 5.6a and b) or the average (figures 5.6c and d) values at ~1033 and ~1076 cm^{-1}. The error bars associated with the averaged absorbance values of diseased samples in figures 5.6c and d were larger than the normal sample values as each mouse could be at a different stage of the disease.

The absorbance data for arthritis also showed a separation at ~1033 cm^{-1} but no appreciable difference in the mannose peak at ~1076 cm^{-1} (figure 5.6b). However, especially for colitis samples, there were clear separations from the normal samples. Moreover, arthritis serum samples displayed an absorption peak at 1292 cm^{-1} which was observed only for arthritis and not for colitis (both DSS and IL10-/-) or metabolic syndrome serum samples. This peak was identified as thymine[106]. It has been reported that, in cases of arthritis, thymidine begins to break down to thymine[115] which explains the increased presence of thymine in the serum.

On deconvolution of the spectra by performing the second derivative on the absorbance values (figure 5.7), one can clearly distinguish between the serum samples representative of intra- (colitic) and extra- (arthritic) intestinal inflammation based on the thymine peak.

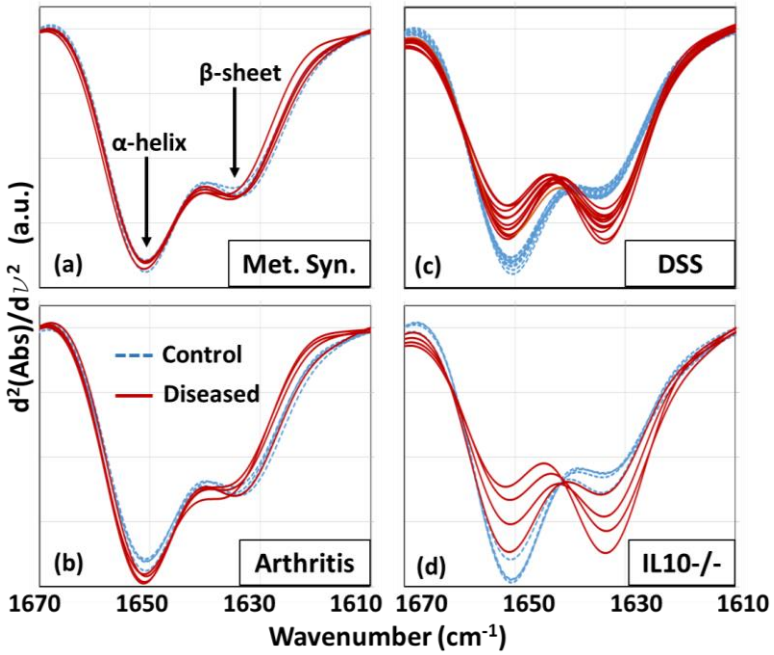

Figure 5.11 *Second derivative of absorbance at the amide I region shows the peaks corresponding to the α–helix and β–sheet whose ratio is always higher in controls than DSS and IL10-/- colitic mice. However, metabolic syndrome and arthritis serum does not show any significant difference in ratio. This indicates that the α–helix to β–sheet ratio is a unique identifier for colitis.*

There was no notable difference in absorbance values for the metabolic syndrome samples and their controls indicating that the presence of metabolic syndrome was not manifested at these spectral markers. The analysis indicated that the increase in glucose peak (~1033 cm^{-1}) was common to colitis and arthritis, but the increase in mannose peak (~1076 cm^{-1}) was unique to colitis.

Cluster and heterogeneity analyses[116], commonly employed in computational biology, were carried out in the spectral range of 1140 to 1000 cm^{-1} to include the glucose (1033 cm^{-1}) and mannose (1076 cm^{-1}) peaks. The input datasets include the 12 DSS induced colitic and 12 control sample spectra. The resulting data is plotted as a heterogeneity dendrogram chart (figure 5.8) indicating that the spectra were correctly grouped together and classified into two clusters, namely control and colitic with a high degree of heterogeneity.

Alpha helices and beta sheets are components of protein secondary structures with vital functions. Alpha helices aid in the binding of DNA and transmembrane spanning[117]. Beta sheets are polypeptide strands woven together with the aid of hydrogen bonding giving the appearance of ribbons or sheets. Their functions include recognition of target binding sites, domain stability and protein folding. Alpha helix and beta sheet are the primary factors deciding the structure of proteins[118] which directly relates to their functions. Figure 5.9 indicates that for colitis irrespective of DSS or IL10-/- models, the alpha helix to beta sheet ratio is always lesser than their controls.

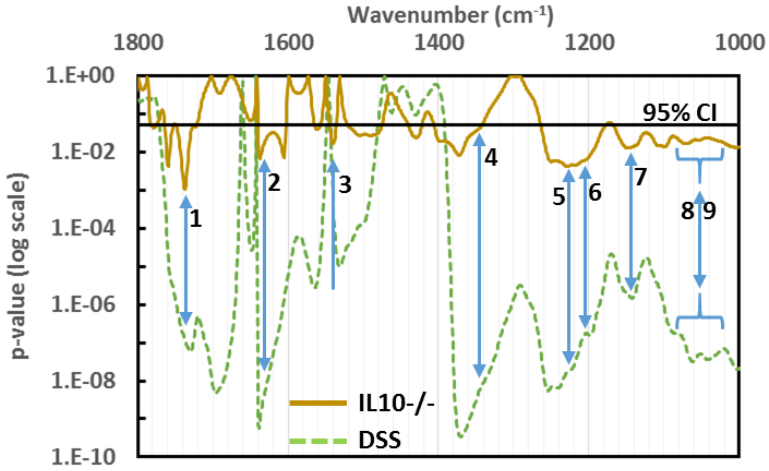

Figure 5.12 *Students t-test p-values calculated for IL10-/- and DSS models. The arrows indicate peaks where colitic samples of both IL10-/- and DSS are separated from their controls with high significance ($p<0.05$, indicated by black line). The corresponding peaks (in cm^{-1}) other than the previously identified mannose (8) and glucose (9) are (1) 1740, (2) 1635, (3) 1540, (4) 1368, (5) 1240, (6) 1206 and (7) 1160.*

Students t-test was performed on the colitic and control samples of IL10-/- and DSS models. Seven additional spectral absorbance peaks (figure 5.10) were chosen as signatures (giving a total of 9 with the previously identified glucose and mannose signatures) with a significance better than 0.05 (i.e. 95% or higher).

These were assigned as C=O stretching of lipids and polysaccharides (1740 cm^{-1}), β-sheet of amide I (1635 cm^{-1}), β-sheet of amide II (1540 cm^{-1}), CH_2 stretching of polysaccharides (1368 cm^{-1}), amide III of collagen (1240 cm^{-1}), collagen (1206 cm^{-1}) and C-O stretching of collagen (1163 cm^{-1}). Increased levels of collagen in serum has been reported[119,120] due to collagen deposition in the mucosal and submucosal layers of the colitis stricken colon[121].

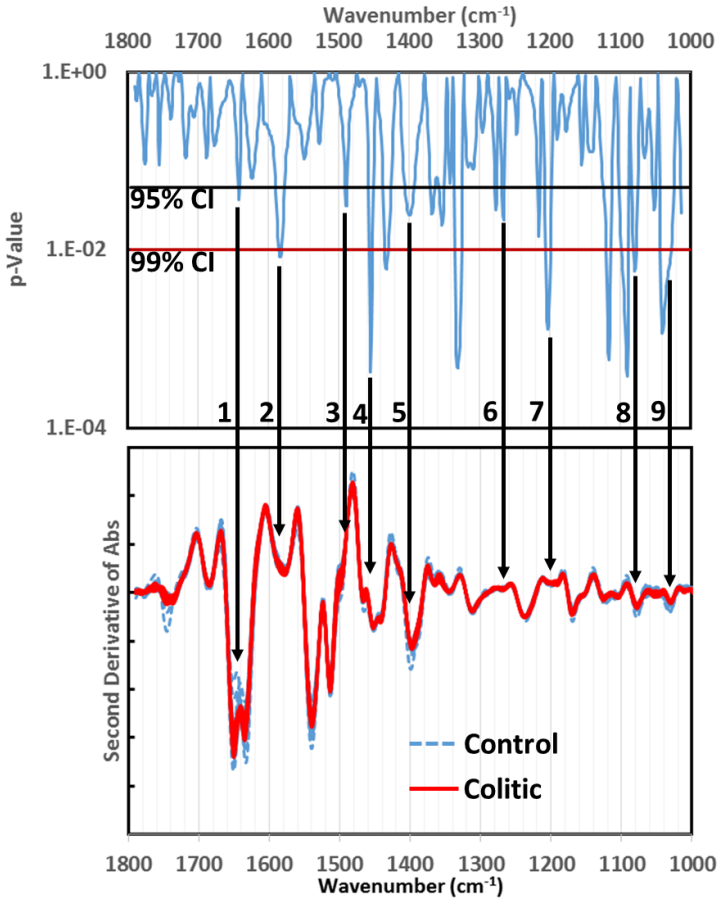

Figure 5.13 *Students t-test p-values calculated for human UC and their control spectra. The arrows indicate frequency positions that coincide with p-values greater than 95% confidence interval and spectral peaks. The corresponding peaks (in cm^{-1}) are (1) alpha helix of amide I, (2) C-C phenyl ring stretch, (3) CH bending vibration, (4) Methyl bending vibration, (5) Methyl symmetric stretching, (6) Phosphate asymetric stretching, (7) Collagen, (8) Mannose and (9) Glucose.*

The next step was to apply the screening technique optimized using mice models to human serum samples. Twelve (12 female and 4 male) ulcerative colitis serum samples were procured

from Boston Biosource, LLC along with their age and gender matched controls. ATR-FTIR screening technique was applied and the same post processing protocols were employed. There appeared to be a large variations in the absorbance spectra as expected causing the overlap of the colitic and control spectra.

However, on applying the second derivative, more statistically significant peaks emerged (figure 5.11). A students' t-test was performed on the two groups to determine the significance of the grouping and separation. The peaks identified as (1) alpha helix of amide I, (2) C-C phenyl ring stretch, (3) CH bending vibration, (4) Methyl bending vibration, (5) Methyl symmetric stretching, (6) Phosphate asymmetric stretching, (7) Collagen, (8) Mannose and (9) Glucose clearly distinguish UC serum samples from controls with $p<0.05$.

5.4 Conclusion

A rapid, simple, cost effective and minimally invasive technique, ATR-FTIR spectroscopy, has been demonstrated as an effective tool to detect colitis in mice serum. The use of a metabolic syndrome mouse model and an arthritis model indicate the specificity of the mannose peak for colitis. More work is currently being done including, a) increased sample sizes, b) specificity of diagnosis to other IBDs such as collagenous and lymphocytic colitis and Crohn's disease, c) calibration of the markers to determine the sensitivity and d) to miniaturize the technique to small devices and with positive human blood trials. In terms of application, this potential technology can be further developed into a personalized diagnostic tool in which patient-to-patient differences in molecular signatures would allow the assessment of disease status and personalized drug management. We can anticipate that this technology could be integrated in a portable device, like the current glucometer, that each patient would wear as a platform to monitor multiple health parameters at the point-of-care, facilitating the creation of bedside technologies for diagnostics

and treatment monitoring for various other medical conditions[95] such as arthritis, viral or bacterial infections, allergies etc including IBD.

REFERENCES

[1] N.D. Mermin, Phys. Today **38** (1985) 38-47.
[2] J. Boussinesq, Théorie analytique de la chaleur: Problèmes généraux, Gauthier-Villars, 1901.
[3] P.R. Griffiths, J.A. De Haseth, Fourier transform infrared spectrometry, John Wiley & Sons, 2007.
[4] R. Gillard, Analyst **88** (1963) 825-828.
[5] N. Berova, K. Nakanishi, Circular dichroism: principles and applications, John Wiley & Sons, 2000.
[6] S.R. Martin, M.J. Schilstra, in, Methods in Cell Biology, Academic Press, 2008, pp. 263-293.
[7] C. JMDAN, L. Lerman, J. Venable, Nature **236** (1972) 67-70.
[8] Compact antenna with circular polarization, Google Patents, 2004.
[9] J. Bailey, A. Chrysostomou, J. Hough, T. Gledhill, A. McCall, S. Clark, F. Ménard, M. Tamura, Science **281** (1998) 672-674.
[10] Y. Lao, A. Perera, H. Wang, J. Zhao, Y. Jin, D. Zhang, J. Appl. Phys. **119** (2016) 105304.
[11] A. Perera, P. Jayaweera, G. Ariyawansa, S. Matsik, K. Tennakone, M. Buchanan, H. Liu, X. Su, P. Bhattacharya, Microelectronics Journal **40** (2009) 507-511.
[12] S. Wolde, Y.-F. Lao, A.U. Perera, Y. Zhang, T. Wang, J. Kim, T. Schuler-Sandy, Z.-B. Tian, S. Krishna, Appl. Phys. Lett. **105** (2014) 151107.
[13] P. Bhattacharya, X. Su, S. Chakrabarti, G. Ariyawansa, A. Perera, (2005).
[14] X. Su, J. Yang, P. Bhattacharya, G. Ariyawansa, A. Perera, (2006).
[15] P. Jayaweera, P.D.P. Pitigala, J.F. Shao, K. Tennakone, A. Perera, P.M. Jayaweera, J. Baltrusaitis, Electron Devices, IEEE Transactions on **57** (2010) 2756-2760.
[16] A. Perera, S. Matsik, P. Jayaweera, K. Tennakone, H. Liu, M. Buchanan, G. Von Winckel, A. Stintz, S. Krishna, Appl. Phys. Lett. **89** (2006) 131118-131118.
[17] Y. Lao, P. Pitigala, A. Perera, H. Liu, M. Buchanan, Z. Wasilewski, K. Choi, P. Wijewarnasuriya, Light-hole and heavy-hole transitions for high-temperature long-wavelength infrared detection, DTIC Document, 2010.
[18] R.C. Jayasinghe, G. Ariyawansa, N. Dietz, A.U. Perera, S.G. Matsik, B.Y. Hongbo, I.T. Ferguson, A. Bezinger, S.R. Laframboise, M. Buchanan, Opt. Lett. **33** (2008) 2422-2424.
[19] M. In, Appl. Phys. Lett. **92** (2008) 111104.
[20] J. Titus, H. Nguyen, Z. Mi, A. Perera, Appl. Phys. Lett. **102** (2013) 121901.
[21] L. Bousse, Sensors Actuators B: Chem. **34** (1996) 270-275.
[22] P. Wang, G. Xu, L. Qin, Y. Xu, Y. Li, R. Li, Sensors Actuators B: Chem. **108** (2005) 576-584.
[23] R. Medzhitov, Nat. Rev. Immunol. **1** (2001) 135-145.
[24] J. Titus, C. Filfili, J.K. Hilliard, J.A. Ward, A.U. Perera, Appl. Phys. Lett. **104** (2014) 243705.
[25] J. Titus, E. Viennois, D. Merlin, A.G. Unil Perera, J. Biophotonics (2016) n/a-n/a.
[26] B. Wang, J. Zhou, T. Koschny, M. Kafesaki, C.M. Soukoulis, Journal of Optics A: Pure and Applied Optics **11** (2009) 114003.
[27] S. Tretyakov, A. Sihvola, L. Jylhä, Photonics and Nanostructures - Fundamentals and Applications **3** (2005) 107-115.

[28] J. Pendry, Science **306** (2004) 1353-1355.
[29] N. Purdie, K.A. Swallows, Analytical chemistry **61** (1989) 77A-89A.
[30] T.A. Keiderling, Current opinion in chemical biology **6** (2002) 682-688.
[31] D. Morrison, T.R. Austin, D. Ivnitski, F. Milanovich, NATO Security through Science Series, Series B: Physics and Biophysics **1** (2005).
[32] T. Nee, S. Nee, Shipboard Infrared Circular Polarization Sensor for Sea-Skimming Missile Detection, DTIC Document, 1999.
[33] Y. He, Y. Zhao, Nanoscale **3** (2011) 2361-2375.
[34] J.D. Driskell, S. Shanmukh, Y. Liu, S.B. Chaney, X.-J. Tang, Y.-P. Zhao, R.A. Dluhy, J. Phys. Chem. C **112** (2008) 895-901.
[35] Y. He, J. Fu, Y. Zhao, Frontiers of Physics **9** (2014) 47-59.
[36] P.R. West, S. Ishii, G.V. Naik, N.K. Emani, V.M. Shalaev, A. Boltasseva, Laser & Photonics Reviews **4** (2010) 795-808.
[37] A.G. Mark, J.G. Gibbs, T.-C. Lee, P. Fischer, Nature materials **12** (2013) 802-807.
[38] J.H. Singh, G. Nair, A. Ghosh, A. Ghosh, Nanoscale **5** (2013) 7224-7228.
[39] G. Larsen, Y. He, W. Ingram, E. LaPaquette, J. Wang, Y.-P. Zhao, Nanoscale (2014).
[40] H. Johnson Singh, A. Ghosh, The Journal of Physical Chemistry C **116** (2012) 19467-19471.
[41] G.K. Larsen, Y. He, J. Wang, Y. Zhao, Advanced Optical Materials **2** (2014) 245-249.
[42] S. Mukherjee, D. Gall, Thin Solid Films **527** (2013) 158-163.
[43] Z.-Y. Zhang, Y.-P. Zhao, Appl. Phys. Lett. **90** (2007) 221501.
[44] J.K. Gansel, M. Wegener, S. Burger, S. Linden, Opt. Express **18** (2010) 1059-1069.
[45] P.L. Polavarapu, The Journal of Physical Chemistry A **109** (2005) 7013-7023.
[46] D.-H. Kwon, P.L. Werner, D.H. Werner, Opt. Express **16** (2008) 11802-11807.
[47] W. Spitzer, D. Kleinman, Phys. Rev. **121** (1961) 1324.
[48] H.P. Nguyen, S. Zhang, K. Cui, X. Han, S. Fathololoumi, M. Couillard, G.A. Botton, Z. Mi, Nano letters **11** (2011) 1919-24.
[49] H.P. Nguyen, K. Cui, S. Zhang, S. Fathololoumi, Z. Mi, Nanotechnology **22** (2011) 445202.
[50] S. Chakrabarti, S. Adhikary, N. Halder, Y. Aytac, A.G.U. Perera, Appl Phys Lett **99** (2011).
[51] G. Ariyawansa, A.G.U. Perera, G.S. Raghavan, G. von Winckel, A. Stintz, S. Krishna, Ieee Photonic Tech L **17** (2005) 1064-1066.
[52] Y.L. Chang, Z.T. Mi, F. Li, Adv Funct Mater **20** (2010) 4146-4151.
[53] K. Domen, K. Horino, A. Kuramata, T. Tanahashi, Appl Phys Lett **71** (1997) 1996-1998.
[54] E.O. Schafer-Nolte, T. Stoica, T. Gotschke, F. Limbach, E. Sutter, P. Sutter, R. Calarco, Appl Phys Lett **96** (2010).
[55] G. Lucovsky, Solar Cells **2** (1980) 431-442.
[56] D.G. Mead, S.R. Lowry, Appl Spectrosc **34** (1980) 167-171.
[57] D.N. Talwar, Appl Phys Lett **97** (2010).
[58] D.W. Berreman, Physical Review **130** (1963) 2193-2198.
[59] K. Jeganathan, R.K. Debnath, R. Meijers, T. Stoica, R. Calarco, D. Grutzmacher, H. Luth, J Appl Phys **105** (2009).
[60] S. Dhara, S. Prasana, A.K. Tyagi, R. Baldev, in, 2011.
[61] T. Azuhata, T. Matsunaga, K. Shimada, K. Yoshida, T. Sota, K. Suzuki, S. Nakamura, Physica B **219-20** (1996) 493-495.

[62] R. Mata, A. Cros, K. Hestroffer, B. Daudin, Phys Rev B **85** (2012).
[63] J.W. Ager, W. Walukiewicz, W. Shan, K.M. Yu, S.X. Li, E.E. Haller, H. Lu, W.J. Schaff, Phys Rev B **72** (2005).
[64] H. Harima, J Phys-Condens Mat **14** (2002) R967-R993.
[65] V. Erukhimovitch, M. Talyshinsky, Y. Souprun, M. Huleihel, in, DNA Viruses, Springer, 2005, pp. 161-172.
[66] G. Hastings, P. Krug, R.L. Wang, J. Guo, H.P. Lamichhane, T. Tang, Y.S. Hsu, J. Ward, D. Katz, J. Hilliard, Analyst **134** (2009) 1462-1471.
[67] F.T. Lee-Montiel, K.A. Reynolds, M.R. Riley, Journal of biological engineering **5** (2011) 16.
[68] S.G. Kazarian, K.L. Chan, Analyst **138** (2013) 1940-51.
[69] J. Hilliard, C. Filfili, I. Patrusheva, P. Fuchs, D. Katz, R. Wang, G. Hastings, M.J. Guo, Y.-S. Hsu, J. Ward, Cell Biosensors: Rapid Detection and Identification of Pathogens Using FTIR Microspectroscopic Spectra, Essen, Germany 2010, 29.
[70] V. Erukhimovitch, E. Bogomolny, M. Huleihil, M. Huleihel, Analyst **136** (2011) 2818-24.
[71] C.S. Ng, H. Kato, T. Fujita, International immunology **24** (2012) 739-49.
[72] W.F. Hawse, M.M. Champion, M.V. Joyce, L.M. Hellman, M. Hossain, V. Ryan, B.G. Pierce, Z. Weng, B.M. Baker, Journal of immunology **188** (2012) 5819-23.
[73] W. Urbaniak-Domagala, in: M.A. Farrukh (Ed.), Advanced Aspects of Spectroscopy, 2012.
[74] Z. Movasaghi, S. Rehman, I.U. Rehman, Appl Spectrosc Rev **43** (2008) 134-179.
[75] A. Bright, T. Renuga Devi, S. Gunasekaran, International Journal of ChemTech Research **2** (2010).
[76] D. Hopwood, The Histochemical journal **1** (1969) 323-360.
[77] F.L. Carson, J.H. Martin, J.A. Lynn, Am. J. Clin. Pathol. **59** (1973) 365-373.
[78] C.H. Fox, F.B. Johnson, J. Whiting, P.P. Roller, J. Histochem. Cytochem. **33** (1985) 845-853.
[79] F. Sjöstrand, R. Baker, J. Ultrastruct. Res. **1** (1958) 239-246.
[80] G. Hastings, R. Wang, P. Krug, D. Katz, J. Hilliard, Biopolymers **89** (2008) 921-30.
[81] L. Barboza, S. Salmen, G. Teran-Angel, D.L. Peterson, L. Berrueta, Cellular immunology **284** (2013) 9-19.
[82] H. Wang, T.A. Kadlecek, B.B. Au-Yeung, H.E. Goodfellow, L.Y. Hsu, T.S. Freedman, A. Weiss, Cold Spring Harbor perspectives in biology **2** (2010) a002279.
[83] C. Cheadle, J. Fan, Y.S. Cho-Chung, T. Werner, J. Ray, L. Do, M. Gorospe, K.G. Becker, BMC genomics **6** (2005) 75.
[84] N.A. de Weerd, S.A. Samarajiwa, P.J. Hertzog, The Journal of biological chemistry **282** (2007) 20053-7.
[85] A. Borroto, I. Arellano, R. Blanco, M. Fuentes, A. Orfao, E.P. Dopfer, M. Prouza, M. Suchanek, W.W. Schamel, B. Alarcon, Journal of immunology **192** (2014) 2042-53.
[86] R. Wang, P. Cherukuri, J. Luo, The Journal of biological chemistry **280** (2005) 11528-34.
[87] D. Hebenstreit, J. Horejs-Hoeck, A. Duschl, Drug news & perspectives **18** (2005) 243-9.
[88] S.G. Kazarian, K.L.A. Chan, Biochimica et Biophysica Acta (BBA) - Biomembranes **1758** (2006) 858-867.
[89] A. Kornbluth, J.F. Marion, P. Salomon, H.D. Janowitz, J. Clin. Gastroenterol. **20** (1995) 280-284.

[90] S. Friedman, P.H. Rubin, C. Bodian, E. Goldstein, N. Harpaz, D.H. Present, Gastroenterology **120** (2001) 820-826.
[91] S. Argov, R.K. Sahu, E. Bernshtain, A. Salman, G. Shohat, U. Zelig, S. Mordechai, Biopolymers **75** (2004) 384-392.
[92] A. Schreyer, H. Rath, R. Kikinis, M. Völk, J. Schölmerich, S. Feuerbach, G. Rogler, J. Seitz, H. Herfarth, Gut **54** (2005) 250-256.
[93] A.J. Sommer, L.G. Tisinger, C. Marcott, G.M. Story, Appl. Spectrosc. **55** (2001) 252-256.
[94] S. Kazarian, K. Chan, The Analyst **138** (2013) 1940-1951.
[95] J. Titus, C. Filfili, J.K. Hilliard, J.A. Ward, A.G.U. Perera, Appl. Phys. Lett. **104** (2014) 243705.
[96] M. Vijay-Kumar, J.D. Aitken, F.A. Carvalho, T.C. Cullender, S. Mwangi, S. Srinivasan, S.V. Sitaraman, R. Knight, R.E. Ley, A.T. Gewirtz, Science **328** (2010) 228-231.
[97] C. Yu, J. Irudayaraj, Biopolymers **77** (2005) 368-377.
[98] R. Kennedy, M. Hoper, K. Deodhar, P. Erwin, S. Kirk, K. Gardiner, Br. J. Surg. **87** (2000) 1346-1351.
[99] J.J. Kim, M.S. Shajib, M.M. Manocha, W.I. Khan, Journal of Visualized Experiments : JoVE (2012) 3678.
[100] H. Laroui, S.A. Ingersoll, H.C. Liu, M.T. Baker, S. Ayyadurai, M.A. Charania, F. Laroui, Y. Yan, S.V. Sitaraman, D. Merlin, PLoS ONE **7** (2012) e32084.
[101] B. Chassaing, J.D. Aitken, M. Malleshappa, M. Vijay-Kumar, Current Protocols in Immunology 15.25. 1-15.25. 14.
[102] M.L. Clapper, H.S. Cooper, W.C.L. CHANG, Acta Pharmacol. Sin. **28** (2007) 1450-1459.
[103] M. Perše, A. Cerar, J. Biomed. Biotechnol. **2012** (2011) 718617-718617.
[104] E. Viennois, B. Xiao, S. Ayyadurai, L. Wang, P.G. Wang, Q. Zhang, Y. Chen, D. Merlin, Lab. Investig. **94** (2014) 950-965.
[105] B. Chassaing, G. Srinivasan, M.A. Delgado, A.N. Young, A.T. Gewirtz, M. Vijay-Kumar, PLoS ONE **7** (2012) e44328.
[106] Z. Movasaghi, S. Rehman, D.I. ur Rehman, Applied Spectroscopy Reviews **43** (2008) 134-179.
[107] C. Petibois, V. Rigalleau, A.-M. Melin, A. Perromat, G. Cazorla, H. Gin, G. Déléris, Clin. Chem. **45** (1999) 1530-1535.
[108] G. Kos, H. Lohninger, R. Krska, Mycotoxin research **19** (2003) 149-153.
[109] M. Ahmad, S. Krishnan, B. Ramakrishna, M. Mathan, A. Pulimood, S. Murthy, Gut **46** (2000) 493-499.
[110] G. Maconi, F. Furfaro, R. Sciurti, C. Bezzio, S. Ardizzone, R. de Franchis, World Journal of Gastroenterology : WJG **20** (2014) 3507-3515.
[111] M. Vijay-Kumar, J.D. Aitken, F.A. Carvalho, T.C. Cullender, S. Mwangi, S. Srinivasan, S.V. Sitaraman, R. Knight, R.E. Ley, A.T. Gewirtz, Science **328** (2010) 228-31.
[112] R. Teague, D. Fraser, J. Clamp, BMJ **2** (1973) 645-646.
[113] H.J. Freeman, Inflammatory Bowel Disease, Taylor & Francis, 1989.
[114] R. Schicho, A. Nazyrova, R. Shaykhutdinov, G. Duggan, H.J. Vogel, M. Storr, J. Proteome Res. **9** (2010) 6265-6273.
[115] P. Nykänen, Scand. J. Immunol. **9** (1979) 477-482.

[116] E. Godehardt, Graphs as structural models: The application of graphs and multigraphs in cluster analysis, Springer Science & Business Media, 2013.
[117] C.I. Branden, Introduction to protein structure, Garland Science, 1999.
[118] W.G. Hol, L.M. Halie, C. Sander, Nature **294** (1981) 532-536.
[119] I.E. Koutroubakis, E. Petinaki, P. Dimoulios, E. Vardas, M. Roussomoustakaki, A.N. Maniatis, E.A. Kouroumalis, J. Clin. Pathol. **56** (2003) 817-820.
[120] P. Koelink, S. Overbeek, S. Braber, M. Morgan, P. Henricks, R.M. Abdul, H. Verspaget, S. Wolfkamp, A. te Velde, C. Jones, Gut **63** (2014) 578-587.
[121] K. Suzuki, X. Sun, M. Nagata, T. Kawase, H. Yamaguchi, V. Sukumaran, Y. Kawauchi, H. Kawachi, T. Nishino, K. Watanabe, Pathol. Int. **61** (2011) 228-238.

APPENDICES

Appendix A

Removal of spectral noise associated with moisture

ATR-FTIR spectral measurements performed using a single reflection ZnSe crystal (Harrick Scientific) exhibited many sharp dips in absorbance. These were identified as absorbance due to moisture present in the ambient air in the sample compartment of the FTIR instrument. This existed since this specific ATR kit did not have the provision for purging of the air. However, this could be rectified if an absorbance spectra of moisture could be added to the composite spectra of the sample and the inherent moisture absorbance. The difficulty here was to determine how much of the moisture absorbance had to be added. This was accomplished by first extracting the absorbance of just moisture by dividing two consecutive background curves that were recorded immediately prior to the sample spectra collection. This moisture spectra will be the best representation of the ambient conditions for that particular sample spectra. This moisture absorbance is then titrated into the sample absorbance with the help of MS Excel software by adding a multiple of a certain factor of moisture absorbance to the sample absorbance. The variation of the slope as a function of wavelength is determined by performing the second derivative of the absorbance data followed by subtracting the square of consecutive absorbance data points. At the optimum condition determined by the multiple factor, the slope variation along the frequency scale will be a minimum as seen in figure A1. This multiple factor is determined by the analytical tool in MS Excel named solver which minimizes the difference in the slope of consecutive data points. This issue was later resolved by employing a diamond ATR unit which had the capability to purge the air inside the unit thus producing spectra devoid of moisture spectral noise.

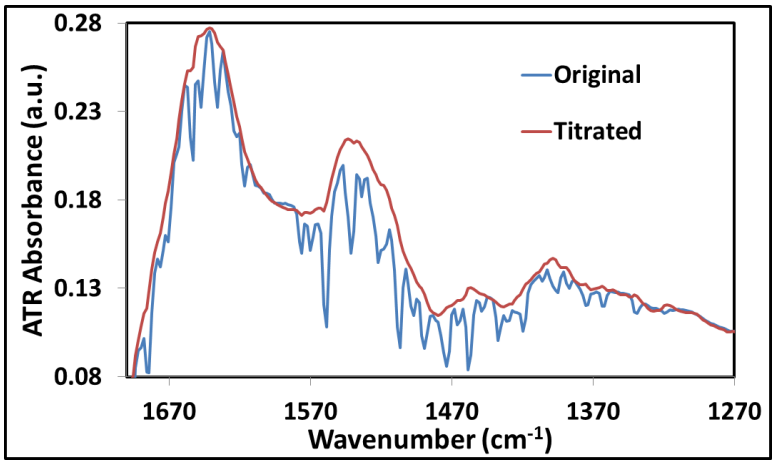

Figure A1 *The ATR spectra of jurkat cells before and after adjusting for the noise spikes due to moisture absorbances by mathematically titrating the moisture absorbance into the sample spectrum while minimizing the slope variations. This moisture issue can be avoided by using an ATR kit that can be purged.*

Appendix B

Protocol for Jurkat cell sample preparation

1- Obtain Jurkat, Clone E6-1 cells (ATCC # TIB-152) in log-phase growth grown in R-10 growth medium (RPMI-1640 supplemented with 10% FBS, 100 U/ml penicillin, and 100 µg/ml streptomycin); count and check for viability by the trypan blue exclusion method (only >95% viability acceptable).

2- Aliquot cells in 1 million cells each in sterile capped 1.5 ml vials, and centrifuge at room temperature for 4 minutes at 800g.

3- Completely remove the growth medium, and replace with 100 µl of either fresh R-10 for control or with R-10 supplemented with 100 ng/ml anti-CD3 antibody (Mabtech).

4- Incubate the cells in a humidified 37□C incubator for 75 minutes with the lids loose for gas exchange.

5- Pool the contents of two vials of the same treatment such that you have 2 million cells per vial.

6- Add 1 ml of ice-cold unsupplemented RPMI-1640 medium to each vial and centrifuge at 800g for 4 minutes.

7- Remove supernatant and wash a second time with 1 ml of ice-cold unsupplemented RPMI-1640 medium. Remove the supernatant completely.

8- Resuspend the pellet (2 million cells) in 16 µl of cold fresh unsupplemented RPMI-1640 medium. Place on ice and transfer to the FTIR lab for immediate reading.

9- For medium controls, supply an aliquot of unsupplemented RPMI-1640 medium and another of medium plus 100 ng/ml of anti-CD3 antibody.

10- Note: treat any additional time points in the same manner described above.

Appendix C

Normalization techniques employed for spectral analysis

Normalization of data is done to enable one to compare one spectrum with another by accounting for the variations due to changes in concentration or size of the sample. The two commonly used normalization techniques in infrared spectroscopy in biology are min-max and vector normalization.

Vector Normalization: This technique is not dependent on any one peak, but rather on the entire spectral region of interest. Each data point in the spectra is first subtracted by the average of all the datapoints. Then all the datapoints are divided by the square root of the sum of squares of all the intensities.

Min-Max Normalization: A baseline offset is first subtracted from the entire spectrum. Then the largest x-value (i.e.) absorbance value is set to be at a maximum of 2 by multiplying each data point with a constant. The commonly used peak for min-max normalization is the amide I since the variations of absorbances at this frequency is minimum.

Appendix D

Characterized human ulcerative colitis samples obtained from Boston Biosource, LLC

Sample	Age at Excision	Sex	BMI	Menopausal Status	Smoking Status	Cigarettes / Day	Alcohol Status	Clinical Diagnoses (other than UC)
1	77	Female	28.35	Post-menopausal	Never Used		Never Used	Hypertension(Status:Ongoing), Hypothyroidism(Status:Ongoing), Seasonal allergies(Status:Ongoing), Hyperlipidemia(Status:Ongoing), Gastroesophageal reflux disease(Status:Ongoing)
2	37	Male	27.1		Never Used		Never Used	
3	20	Male	22.5		Never Used		Never Used	
4	61	Male	25.7		Never Used		Never Used	Osteoarthritis(Status:Ongoing), Hypertension(Status:Ongoing), Gastroesophageal reflux disease(Status:Ongoing)
5	57	Female	27.29	Post-menopausal	Never Used		Never Used	Fibromyalgia(Status:Ongoing), Osteoporosis(Status:Ongoing), Osteoarthritis(Status:Ongoing)
6	84	Male	24.65		Never Used		Never Used	ulcer(Status:Ongoing), Angina(Status:Ongoing), Hyperlipidemia(Status:Ongoing), Ischemic heart disease(Status:Ongoing)
7	23	Female	23.34	Pre-menopausal	Never Used		Never Used	
8	72	Female	29.37	Post-menopausal	Previous Use	6	Occasional Use	Osteoarthritis(Status:Ongoing), Kidney failure(Status:Ongoing), Myocardial infarction(Status:Past), Irritable bowel syndrome(Status:Ongoing), Hypertension(Status:Ongoing), High cholesterol(Status:Ongoing), Hysterectomy(Status:Ongoing)
9	23	Female	25.15	Pre-menopausal	Previous Use	2	Occasional Use	
10	41	Female	26.02	Post-menopausal	Never Used		Never Used	Hypertension(Status:Ongoing), Allergic rhinits(Status:Ongoing), Fibromyalgia(Status:Ongoing)
11	40	Female	33.79	Pre-menopausal	Never Used		Never Used	Fibromyalgia(Status:New), Anxiety(Status:Ongoing), Migraines(Status:Recurrent)
12	54	Female	23.19	Post-menopausal	Current Use	10	Occasional Use	